https://dx.doi.org/10.1016/j.corsci.2020.108900

Manuscript Details

Manuscript number	CORSCI_2020_693_R3
Title	Multi-Phase-Field Modeling of Localized Corrosion involving Galvanic Pitting and Mechano-electrochemical Coupling
Article type	Full Length Article

Abstract

A new multi-phase-field (multi-PF) model is proposed to study a complex localized corrosion process that involves mechano-electrochemical coupling, anodic dissolution, insoluble depositions (IDs) formation, and resulted Galvanic-pitting corrosion. Based on a quantitative investigation into the effects of Cl- concentration, pH value, mechanical loading, and electric field, we reveal the autocatalytic process of pitting assisted by increasingly aggressive chemical environment and concentrated stress and study how the external electric field can arrest assisted corrosion and prolong service lifetime. The proposed model can be a useful tool for the lifetime management of metallic components serving in ocean or other more aggressive environments.

Keywords	Multi-Phase-Field Model; Localized Corrosion; Galvanic-Pitting; Mechano-electrochemical Coupling.
Taxonomy	Complex Physical Systems, Modeling in Materials Science
Corresponding Author	Haihui Ruan
Corresponding Author's Institution	HKPolyU
Order of Authors	Chen Lin, Haihui Ruan

Highlights

- A galvanic pitting and mechano-electrochemical multi-phase-field model is proposed
- Occluded cell corrosion process is numerically studied
- Pitting corrosion is assisted by aggressive chemical environment and concentrated stress
- External electric field can arrest assisted corrosion and prolong service lifetime

Multi-Phase-Field Modeling of Localized Corrosion involving Galvanic Pitting and Mechano-electrochemical Coupling

Chen Lin[a], Haihui Ruan[a, *]

a. Department of Mechanical Engineering, The Hong Kong Polytechnic University, Hong Kong, China

Abstract

A new multi-phase-field (multi-PF) model is proposed to study a complex localized corrosion process that involves mechano-electrochemical coupling, anodic dissolution, insoluble depositions (IDs) formation, and resulted Galvanic-pitting corrosion. Based on a quantitative investigation into the effects of Cl^- concentration, pH value, mechanical loading, and electric field, we reveal the autocatalytic process of pitting assisted by increasingly aggressive chemical environment and concentrated stress and study how the external electric field can arrest assisted corrosion and prolong service lifetime. The proposed model can be a useful tool for the lifetime management of metallic components serving in ocean or other more aggressive environments.

Keyword: Multi-Phase-Field Model; Localized Corrosion; Galvanic-Pitting; Mechano-electrochemical Coupling.

* Corresponding author Tel.: + 852 2766 6648, Fax: +852 2365 4703, E-mail address: haihui.ruan@polyu.edu.hk

1 Nomenclature

$\mathbf{p}$	Set of order parameters
$\mathbf{c}$	Set of concentration variables
$\boldsymbol{\varphi}$	Electric field
$\mathbf{d}$	Displacement vector
$\boldsymbol{\varepsilon}^{\mathrm{e}}$	Elastic strain
$\mathbf{D}^{\mathrm{e}}$	Elastic stiffness matrix
$\boldsymbol{\sigma}$	Stress tensor
K_{ij}	Scale factor of interfacial energy density
ζ_{ij}	Interfacial thickness between phases i and j
S_{ij}	Interfacial energy density between phases i and j
H_{ij}	Height of energy barrier between phases i and j
r	Reaction rate
μ	Chemical potential
Λ	Driving force of the reaction
L	Coefficient of the contribution of interfacial energy
κ	Coefficient of the contribution of reaction kinetics
D	Diffusion coefficient
ε	Electric conductivity of medias

Introduction

Ocean energy, involving the energy carried by ocean waves, tides, salinity, and ocean temperature differences, has been regarded as one of the most sustainable energy sources. It is estimated that over 75 TW power can be harvested from ocean around the world, which is equivalent to the power generating from 75,000 nuclear reactors [1, 2]. Large-scale commercial exploitation of ocean energy, as a supplementary or replacement of fossil energy sources, could be a solution to the great problems facing mankind, such as energy crisis, greenhouse gas emissions leading to global warming, and environmental degradation. Therefore, various ocean-power generators, based on either electromagnetism or triboelectricity, have been proposed. In particular, the newly-invented triboelectric energy generators (TENGs) [3 – 6], having high energy conversion efficiency up to 70% at low frequency (<1 Hz), could be a promising solution to harvest the vast energy carried by ocean waves. However, the service lifetime of an ocean power generator would inevitably be restricted by the severe electrochemical corrosion in the seawater environment, which leads to degradation in the integrity and durability of metallic components, such as turbines and electrode. While corrosion-induced repairs and replacements have already led to a huge economic burden in many countries (for example, it amounted to approximately 3.34% of GDP in 2018 in China [7].), it is expected that the large-scale exploitation of ocean power plants would further increase the burden.

To resist corrosion, metallic components are usually alloyed with active-passive metals

such as aluminum or chromium to form an oxide-based passive film. However, the dissolution or breakdown of passive film leads to extremely localized corrosion [8 – 10]. Understanding a localized corrosion is very difficult because it involves complex interplay among many chemical processes, such as the transports of corrosive substances, hydrolysis, precipitation and accumulation of corrosion products, as well as the resulting Galvanic-pitting corrosion. In addition, a metallic component is generally subject to mechanical loading, wherein the local stress and strain concentration around a progressively changing pit can accelerate the localized corrosion and also increase the risk of other corrosion phenomena such as stress corrosion cracking initiation at the pitting site. Because it is difficult to experimentally differentiate and determine the effect of each individual factor in the highly heterogeneous and strongly coupled corrosion process, theoretical and numerical models are needed especially when an active corrosion control and protection through electrochemical means could be implemented in a power plant.

The theoretical and numerical investigations of corrosion started with the assumption of steady-state corrosion process, *i.e.*, reactions are assumed to be homogenous in an electrolyte. These investigations illuminated the effects of chemical environment, such as Cl^- concentration and pH value, which can be found in the studies by McCafferty *et al*. [11], Galvele [12], Sharland *et al*. [13], Guseva *et al*. [14], and Deshpande *et al*. [15]. To enable a theoretical treatment, early models assume a fixed corrosion geometry. With the development of computational approaches, the movement of corrosion boundary can be resolved by using

the finite volume method (FVM) [16], finite element method (FEM) [17], extended finite element method (XFEM) [18], nonlocal peri-dynamic (PD) modeling [19, 20], cellular automata (CA) modeling [21 – 24] and phase-field (PF) method [25 – 28]. In FEM and XFEM based models, the corrosion boundary is a sharp interface. Therefore, additional algorithms, such as the remeshing or mesh moving scheme for FEM-based models and the interface tracking scheme for XFEM-based models, are required, which significantly affect the accuracy and convergence of numerical simulations. Alternatively, the FVM, PD, CA and PF methods does not involve sharp interfaces. Among them, the PF model assuming diffusive interfaces is one of the most convenient method to capture a morphology evolution. With a one-dimensional (1D) PF model, Xiao *et al*. [25] investigated crevice corrosion of iron in saltwater, wherein the effects of overpotential and pH value were revealed. Ansari *et al*. [26] then extended Xiao's model to a 2D scenario; Mai *et al*. [27] employed the Allen–Cahn equation with a current-density-dependent reaction kinetics parameter in their PF model to describe the migration of reaction front; and Chadwick *et al.* [28] suggested a boundary-smoothening method in their PF model to describe the morphology evolution of a corrosion pit.

While the aforementioned models have been capable of unveiling a detailed corrosion process, a more comprehensive model, including all the relevant physical, chemical, and mechanical processes, should be required to make the numerical framework applicable to realistic scenarios. It is noted that the Galvanic coupling inevitably occurs in a localized corrosion process and the formation of insoluble depositions (IDs) have a very significant

influence on the local electrochemical environment. Therefore, some attempts have been made to address these problems. Employing FEM, Yin *et al.* [29] and Wang *et al.* [30] investigated the Galvanic-pitting corrosion induced by cathodic IDs. In these models, reactions occurred in the electrolyte were assumed to be homogenous; a moving mesh technique was employed to describe the anodic dissolution; and the blocking and hindrance effects of the predefined IDs were revealed. Treating cathodic reactions as boundary conditions, Mai *et al.* [31] and Lin *et al.* [32] proposed PF models to study the coupling of Galvanic corrosion and pitting, in which the cathode was assumed to be a fixed boundary and the evolution of IDs was not involved. To involve the evolution of IDs, Ansari *et al.* [33] developed a multi-phase-field (multi-PF) model with IDs being one of the phases. In this model, the coupled Galvanic corrosion was not incorporated and the description of the reactions in the electrolyte is incomplete, for example, the hydrolysis of metal-chloride is omitted and as such the effect of Cl^- concentration cannot be revealed.

Nearly all metallic components are used to withstand mechanical loadings. For example, in an ocean power plant, mechanical loadings could be externally applied in the form of irregular ocean flow, wave and wind etc. Furthermore, inherent residual stresses could be induced in a fabrication process involving heat-treatment, machining, and/or cold working. Many experimental investigations have indicated the nontrivial stress effect on a corrosion process [34 – 39]. For example, Wang *et al.*[35] and Kim [38] found that the open circuit potential reduced with the increase in the applied stress; Ren *et al.*[34], Wang *et al.*[35] and

Yang *et al.* [37] observed an increase in the corrosion rate (or corrosion current) when the applied mechanical loading increased. Therefore, the mechano-electrochemical coupling must be involved in modelling corrosion. Referring to the linear relation between free energy and the pressure, Gutman [40] suggested the additional stress term in chemical potential. Sarkar *et al.* [41] analytically studied the effects of stress and surface curvature on corrosion rate with the assumption that the current density is dependent on them. Assuming that the stress-dependent current density follows Gutman's theory [40], Wang *et al.* [21] and Fatoba *et al.* [23] establish their numerical model of corrosion based on the FEM-CA method, that is, the governing equations are solved by FEM and the movement of a corrosion front is described by the CA method. However, CA parameters are not electrochemical quantities but prescribed probabilities [24], which are difficult to determine in application. Jafarzadeh *et al.* [19] assumed a similar stress-dependent current density formulation based on Gutman's theory [40] and solved the problem based on the PD method. The PF model of mechano-electrochemical coupling was proposed by Lin *et al.* [32], who expressed the reaction kinetics as a generalized Butler-Volmer (BV) equation involving chemical potential, electrostatic field, interface energy, and mechanical energy.

To the best of our knowledge, a theoretical or numerical model has not been available to describe all the complexities discussed above (i.e., the formation of IDs, the Galvanic-pitting corrosion, and the mechano-electrochemical coupling) although separate efforts have been made. Therefore, we feel obliged to develop a new multi-PF model to deal with them. In this

work, we considered the corrosion of iron to exemplify the new model. Nevertheless, the theoretical framework should be extensible to describe the corrosion behaviors in other metallic materials, if the chemical processes in them have been well characterized. In the following, we start with the thermodynamics framework that formulates the Helmholtz free energy as the sum of chemical potential, interfacial energy, electrostatic potential energy, and mechanical strain energy. The anodic dissolution and ID formation are regarded as phase transformations and described by Allen-Cahn equations. With the involvement of the Nernst-Planck, Poisson, and stress-equilibrium equations, the complete set of multi-PF equations describes the effects of electric field, Cl^- concentration, pH value and the hindrance of cathodic IDs, as well as the two types of couplings, *i.e.*, Galvanic-pitting and mechano-electrochemical, in a localized corrosion.

2. Methodology

2.1 Corrosion mechanism

Fig. 1

The occluded cell corrosion, as illustrated in Fig. 1, is regarded as one of the most dangerous localized corrosions that could occur in the ocean environment. It starts with a local breakdown of the passive film, which leads to the development of a corrosion pit in seawater. Under the impact of aggressive ions, such as Cl^-, H^+, the metal, i.e., *Fe* in this study, is corroded and releases cations (Fe^{2+}) into seawater, which undergo complex reactions with Cl^-, H^+, OH^-

and form various corrosion products. These reactions can be expressed as:

$$Fe_{(s)} \rightarrow Fe^{2+} + 2e^{-}, \tag{1.a}$$

at the anode (*Fe*)-electrolyte interface,

$$Fe^{2+} + 2Cl^{-} \rightleftharpoons FeCl_{2(ppt)}, \tag{1.b}$$

$$FeCl_{2(ppt)} + 2H_2O \rightleftharpoons Fe(OH)_{2(ppt)} + 2Cl^{-} + 2H^{+}, \tag{1.c}$$

$$Fe^{2+} + 2OH^{-} \rightarrow Fe(OH)_{2(ppt)}, \tag{1.d}$$

in the electrolyte, and

$$4e^{-} + 2H_2O + O_2 \rightarrow 4OH^{-}, \tag{1.e}$$

$$2e^{-} + 2H^{+} \rightarrow H_2 \uparrow, \tag{1.f}$$

$$Fe(OH)_{2(ppt)} \rightarrow Fe(OH)_{2(s)}, \tag{1.g}$$

at the electrolyte-IDs interface. In the above formulae, the subscript "*s*" and "*ppt*" represent solid-state products and the products precipitated from seawater, respectively. The thermodynamically stable products of hydrolysis, e.g., $Fe(OH)_2$, may deposit near corrosion pit, forming IDs, which blocks the pit and leads to an occluded cell corrosion. With the formation of an occluded cell, the solution within the corresponding pit become increasingly acidic and has a high concentration of Cl^-, which is the result of hydrolysis (*i.e.*, Eq. (1.c)) and electric-field assisted diffusion from outside. The acidic environment and high concentration of Cl^- further lead to an accelerated local corrosion, which is one of the most significant causes of catastrophic failure of metals serving in the ocean environment.

2.2. Thermodynamics

To establish a theoretical description of the aforementioned corrosion process, let us express the Helmholtz free energy, F, of the concerned system, Ω, as:

$$F = \int_{\Omega} f\left(\mathbf{p}, \nabla\mathbf{p}, \mathbf{c}, \boldsymbol{\varphi}, \mathbf{d}\right) d\omega, \tag{2}$$

where f, $d\omega$, $\mathbf{p}$, and $\mathbf{c}$ denote the free energy density, infinitesimal volumetric element, set of order parameters, and set of concentration variables, respectively, $\boldsymbol{\varphi}$ and $\mathbf{d}$ represent the electric and displacement fields, respectively. The order parameters, $\mathbf{p}$, and concentrations, $\mathbf{c}$, are further expressed as:

$$\mathbf{p} = \left\{p_1, p_2, p_3\right\} = \left\{c_{Fe_{(s)}} \Big/ c^{\max}_{Fe_{(s)}}, c_{Fe(OH)_{2(s)}} \Big/ c^{\max}_{Fe(OH)_{2(s)}}, 1 - p_1 - p_2\right\}, \tag{3.a}$$

$$\mathbf{c} = \left\{c_{Na^+}, c_{Cl^-}, c_{H^+}, c_{OH^-}, c_{Fe^{2+}}, c_{e^-}, c_{FeCl_{2(ppt)}}, c_{Fe(OH)_{2(ppt)}}, c_{O_2}\right\}, \tag{3.b}$$

respectively, where p_1, p_2, and p_3 designate the anodic iron, cathodic IDs and electrolyte, respectively. In Eq. (3.a), $c_* \big/ c^{\max}_*$ $\left(* = Fe_{(s)} \text{ or } Fe\left(OH\right)_{2(s)}\right)$ represents a dimensionless concentration, where the superscript "max" indicates the maximum molar concentration in the corresponding phase. Letting p_1 and p_2 be the dimensionless concentration is to ensure that either of them is unity in the corresponding solid phase and zero in the other solid phase. To designate the liquid electrolyte phase, we use $p_3 = 1 - p_1 - p_2$, as expressed in Eq. (3.a), namely, p_3 is zero in solid phase but unity in electrolyte.

Following previous theoretical works on corrosion [32], the free energy density, f, is treated as a sum of the interface energy density, f^{Int}, chemical potential energy density, f^{chem}, electric potential energy density, f^{elec}, and mechanical energy density, f^{mech}, namely:

$$f\left(\mathbf{p},\nabla\mathbf{p},\mathbf{c},\boldsymbol{\varphi},\mathbf{d}\right)=f^{\text{int}}\left(\mathbf{p},\nabla\mathbf{p}\right)+f^{chem}\left(\mathbf{p},\mathbf{c}\right)+f^{elec}\left(\mathbf{c},\boldsymbol{\varphi}\right)+f^{mech}\left(\mathbf{p},\mathbf{d}\right). \tag{4}$$

These energetic terms are further formulated hereunder.

Following Kundin *et al.* [42], the interfacial energy density is expressed as:

$$f^{\text{int}}\left(\mathbf{p},\nabla\mathbf{p}\right)=\sum\nolimits_{i,j>i}^{n=3}\left(\frac{K_{ij}}{2}\left|p_j\nabla p_i-p_i\nabla p_j\right|^2\right), \tag{5}$$

where K_{ij} is the scale factor of interfacial energy density for the interface between phases i and j. In the use of a diffusive interface with the finite thickness, ζ_{ij}, to approximate a sharp (zero thickness) interface with the interface energy (per unit area), S_{ij}, it is derived that $K_{ij}=\mathsf{S}_{ij}\zeta_{ij}$ [43].

The chemical potential energy density f^{chem} gives rise to the driving forces of the diffusions of reactants and products, which involves the energy barrier to separate disparate phases. It is expressed as:

$$\begin{aligned} f^{chem}\left(\mathbf{p},\mathbf{c}\right)=&\sum\nolimits_{i,j>i}^{n=3}\left(H_{ij}p_i^2p_j^2\right)+\sum_{*}\left(c_*RT\ln\left(c_*/c_*^{\max}\right)+c_*\left(\mu_*^0-RT\right)\right)\\ &*\in\left\{Na^+,Cl^-,H^+,OH^-,Fe^{2+},FeCl_{2(ppt)},Fe\left(OH\right)_{2(ppt)},O_2\right\}\end{aligned}. \tag{6}$$

In Eq. (6), the first term on the right-hand side is the sum of double-well energetic functions [44] to ensure that stable phases i and j are separated by the energy barrier H_{ij}, which can be related to the interfacial characteristics as $H_{ij}=18\mathsf{S}_{ij}/\zeta_{ij}$ [43]. The second term is the summation of the contributions from all diffusible substances in the system, which follows the expression of chemical potential of diffusible substances in an ideal solution [45]. Therein, R, T and μ_*^0 are the ideal gas constant, thermodynamic temperature, and standard chemical

potential, respectively.

The electric potential energy density, resulting from conservative Coulomb forces between different charged particles, is expressed as:

$$f^{elec}\left(\mathbf{c},\boldsymbol{\varphi}\right)=\sum_{*}\varphi F n_{*}c_{*},\ \ *\in\left\{Na^{+},Cl^{-},H^{+},OH^{-},Fe^{2+},e^{-}\right\}. \tag{7}$$

where φ is the electric potential; F is the Faraday constant; n is the charge number.

Finally, the free energy density due to mechanical stresses is expressed as:

$$f^{mech}\left(\mathbf{p},\mathbf{d}\right)=h\left(p_1\right)f^{mech}_{Fe_{(s)}}+h\left(p_2\right)f^{mech}_{Fe(OH)_{2(s)}}, \tag{8}$$

where $h(x)$ is the continuous interpolation function to cope with the material discontinuity between different phases. Different form of $h(x)$ leads essentially to different types of PF model. Herein, we set $h\left(x\right)=x^3\left(10-15x+6x^2\right)$ because of its simplicity in guaranteeing minimum free energy at p_i = 0 and 1 (cf. [46]). $f^{mech}_{*}=\left(\boldsymbol{\varepsilon}^{\mathrm{e}}\right)^{T}\cdot\left(\mathbf{D}_{*}\boldsymbol{\varepsilon}^{\mathrm{e}}\right)\big/2$ $\left(*\in\left\{Fe_{(s)},Fe\left(OH\right)_{2(s)}\right\}\right)$ is the mechanical energy density of a solid phase with $\mathbf{D}$ and $\boldsymbol{\varepsilon}^{\mathrm{e}}$ being the stiffness matrix and elastic strain tensor, respectively. The latter is obtained from the geometric relation: $\boldsymbol{\varepsilon}^{\mathrm{e}}=\left\{\varepsilon^{\mathrm{e}}_{ij}\right\}=\left\{\left(\partial d_i/\partial x_j+\partial d_j/\partial x_i\right)\big/2\right\}$ $\left(i=1,2,3;\ j=1,2,3\right)$ wherein we have assumed small deformation. In present simulation, we assume that the ID phase ($Fe(OH)_{2(s)}$) is porous and fragile, which is unable to withstand mechanical loading. In this case, Eq. (8) is reduced to:

$$f^{mech}\left(\mathbf{p},\mathbf{d}\right)=h\left(p_1\right)f^{mech}_{Fe_{(s)}}. \tag{9}$$

2.3. Reaction kinetics

For a generalized reaction expressed as: $\sum n_i R_i^{X_i}\rightarrow\sum m_j P_j^{Z_j}$, the reaction rate, r, can

be defined as [47]:

$$r = -\frac{1}{n_i}\frac{\partial c_{R_i^{X_i}}}{\partial t} = \frac{1}{m_j}\frac{\partial c_{P_j^{Z_j}}}{\partial t}, \tag{10}$$

where R_i and P_j symbolize reactants and products respectively, n_i (or m_j) and X_i (or Z_j) denote the stoichiometric number and charge number, respectively. In a reactive system, the forward and backward reactions take place simultaneously, leading to the net reaction rate:

$$r = \overset{\mathsf{r}}{r} - \overset{\mathsf{s}}{r} = k^0\left(e^{-\left(\mu^{TS}-\mu^R\right)/RT} - e^{-\left(\mu^{TS}-\mu^P\right)/RT}\right), \tag{11}$$

where $\overset{\mathsf{r}}{r}$ and $\overset{\mathsf{s}}{r}$ represent the forward and backward reaction rates, respectively. They are further expressed in the Arrhenius form in Eq. (11), where k^0 is the rate coefficient; μ^R, μ^P are the chemical potentials of reactants and products, respectively; μ^{TS} is the chemical potential at the transition state. For a reaction involving multiple reactants and products, μ^R and μ^P, are $\mu^R = \sum_i n_i \mu_{R_i^{X_i}}$ and $\mu^P = \sum_j n_j \mu_{P_j^{Z_j}}$, respectively, where the chemical potential, μ_*, is the variational derivative of the total free energy, F, with respect to the concentration, c_*.

The chemical potential can also be separated into the activity, a_*, and excess chemical potential, μ_*^{ex}, of a specie in the form of $\mu_* = RT\ln a_* + \mu_*^{\mathrm{ex}}$. Thus, the chemical potentials, μ^R and μ^P, can respectively be recast as:

$$\mu^R = RT\ln\left(\prod_i \left(a_{R_i^{X_i}}\right)^{n_i}\right) + \sum_i n_i \mu_{R_i^{X_i}}^{\mathrm{ex}}, \tag{12.a}$$

$$\mu^P = RT\ln\left(\prod_j \left(a_{P_j^{Z_j}}\right)^{n_j}\right) + \sum_j n_j \mu_{P_j^{Z_j}}^{\mathrm{ex}}. \tag{12.b}$$

The chemical potential at the transition state, μ^{TS}, is defined following Bazant [48] as:

$$\mu^{TS} = RT \ln a^{TS} + \rho \sum_i n_i \mu^{\text{ex}}_{R_i^{X_i}} + (1-\rho) \sum_j n_j \mu^{\text{ex}}_{P_j^{Z_j}} , \tag{13}$$

where a^{TS} is the activity of reaction at the transition state; ρ is the asymmetry parameter, which is approximately a constant between zero and one for various reactions [49].

According to the definition of Bazant [48], the activity is only concentration dependent, defined as:

$$a_* = \exp\left(\frac{1}{RT} \left(\frac{\delta\left(\int_\Omega \left(f^{chem} + f^{\text{int}} \right) d\omega \right)}{\delta c_*} - \mu_*^0 \right) \right). \tag{14}$$

Correspondingly, the excess chemical potential, μ_*^{ex}, is:

$$\mu_*^{\text{ex}} = \frac{\delta\left(\int_\Omega f - f^{chem} - f^{\text{int}} d\omega \right)}{\delta c_*} + \mu_*^0 , \tag{15}$$

which involves the contributions of mechanical energy, electric potential, and standard chemical potential.

For the anodic dissolution: $Fe_{(s)} \rightarrow Fe^{2+} + 2e^-$ (Eq. (1.a)) occurring at the metallic electrode-electrolyte interface, the reaction rate, $r_{Fe_{(s)} \rightarrow Fe^{2+}}$, can be expressed as (see Appendix A for derivation):

$$r_{Fe_{(s)} \rightarrow Fe^{2+}} = \kappa_{Fe_{(s)} \rightarrow Fe^{2+}} \left(\exp\left(\frac{\mu_{13}^{\text{int}}}{RT} \right) \exp\left(\frac{(1-\rho)\Lambda_{cor}}{RT} \right) - \frac{c_{Fe^{2+}}}{c_{Fe^{2+}}^{\max}} \exp\left(-\frac{\rho \Lambda_{cor}}{RT} \right) \right), \tag{16}$$

where κ is the scaled reaction rate, μ_{13}^{int} is the chemical potential resulting from the electrode-electrolyte interface energy, and Λ_{cor} is the driving force of the reaction. They are expressed as:

$$\kappa_{Fe_{(s)} \rightarrow Fe^{2+}} = \frac{k^0_{Fe_{(s)} \rightarrow Fe^{2+}}}{a^{TS}_{Fe_{(s)} \rightarrow Fe^{2+}}} , \tag{17.a}$$

$$\mu_{13}^{\text{int}} = -\frac{1}{c_{Fe_{(s)}}^{\max}}\left(K_{13}\left(p_3\nabla p_1^2 - p_1\nabla p_3^2\right) + 2H_{13}p_1p_3\left(p_1 - p_3\right)\right), \tag{17.b}$$

and

$$\Lambda_{cor} = \frac{\partial f_{mech}}{c_{Fe_{(s)}}^{\max}\partial p_1} + \frac{V_m}{3}\left|tr\left(\sigma\right)\right| - \mu_{Fe^{2+}}^{0} + 2F\left(\varphi_M - \varphi_L\right), \tag{17.c}$$

respectively. In Eq. (17.c), V_m is the molar volume of the load-bearing solid phase, $\left|tr\left(\boldsymbol{\sigma}\right)\right| = \left|\sigma_{11} + \sigma_{22} + \sigma_{33}\right|$ is the trace of the stress tensor reflecting the effect of hydrostatic stress [40], and φ_M and φ_L represent the electric potentials in metallic electrode and electrolyte, respectively. Note that the electric potential difference $\varphi_M - \varphi_L$ at the electrode-electrolyte interfacial renders the influence of electric field on corrosion, namely, it is possible to slow down a corrosion process by applying appropriate external electric potential. For those who are familiar with BV equation, it is noted that the reaction rate equation (16) may also be recast in the BV form, in which the overpotential will be related to diffusivity, electric field, interfacial energy, and mechanical stress (see our previous work ref. [32] or Appendix B). In Eq. (16), the contribution from the interfacial energy, μ_{13}^{int}, is much smaller than RT. Therefore, the reaction rate can be recast as:

$$r_{Fe_{(s)}\to Fe^{2+}} \approx L_{Fe_{(s)}\to Fe^{2+}}\mu_{13}^{\text{int}} + \kappa_{Fe_{(s)}\to Fe^{2+}}\left(\exp\left(\frac{\left(1-\rho\right)\Lambda_{cor}}{RT}\right) - \frac{c_{Fe^{2+}}}{c_{Fe^{2+}}^{\max}}\exp\left(-\frac{\rho\Lambda_{cor}}{RT}\right)\right), \tag{18.a}$$

$$L_{Fe_{(s)}\to Fe^{2+}} = \frac{\kappa_{Fe_{(s)}\to Fe^{2+}}}{RT}\exp\left(\frac{\left(1-\rho\right)\Lambda_{cor}}{RT}\right), \tag{18.b}$$

where L is regarded as the coefficient scaling the influence of interface on the reaction rate.

For deposition: $Fe(OH)_{2(ppt)} \rightarrow Fe(OH)_{2(s)}$ at ID-electrolyte interfaces, the reaction rate

can be derived in a similar manner as:

$$r_{Fe(OH)_{2(ppt)}\to Fe(OH)_{2(s)}} = -L_{Fe(OH)_{2(ppt)}\to Fe(OH)_{2(s)}}\mu_{23}^{\text{int}} + \kappa_{Fe(OH)_{2(ppt)}\to Fe(OH)_{2(s)}}\left(\left(\frac{c_{Fe(OH)_{2(ppt)}}}{c_{Fe(OH)_{2(ppt)}}^{\max}}\right)\exp\left(\frac{(1-\rho)\Lambda_{dep}}{RT}\right)-\exp\left(-\frac{\rho\Lambda_{dep}}{RT}\right)\right), \quad (19)$$

where

$$L_{Fe(OH)_{2(ppt)}\to Fe(OH)_{2(s)}} = \frac{\kappa_{Fe(OH)_{2(ppt)}\to Fe(OH)_{2(s)}}}{RT}\exp\left(\frac{(1-\rho)\Lambda_{dep}}{RT}\right), \quad (20.a)$$

$$\kappa_{Fe(OH)_{2(ppt)}\to Fe(OH)_{2(s)}} = \frac{k^0_{Fe(OH)_{2(ppt)}\to Fe(OH)_{2(s)}}}{a^{TS}_{Fe(OH)_{2(ppt)}\to Fe(OH)_{2(s)}}}, \quad (20.b)$$

$$\mu_{23}^{\text{int}} = -\frac{1}{c_{Fe(OH)_{2(s)}}^{\max}}\left(K_{23}\left(p_3\nabla p_2^2 - p_2\nabla p_3^2\right)+2H_{23}p_2p_3\left(p_2-p_3\right)\right), \quad (20.c)$$

and

$$\Lambda_{dep} = \mu^0_{Fe(OH)_{2(ppt)}}, \quad (20.d)$$

where the subscript "*dep*" denotes deposition.

2.4. Governing equations

Because the order parameter, p_1, represents the normalized concentration of iron. It can be related to the reaction rate in the form of $\partial p_1/\partial t \sim -r_{Fe_{(s)}\to Fe^{2+}}\Big/c_{Fe_{(s)}}^{\max}$. The exact governing equation for p_1 should be expressed as:

$$\frac{\partial p_1}{\partial t} = \frac{L_{Fe_{(s)}\to Fe^{2+}}}{\left(c^{\max}_{Fe_{(s)}}\right)^2}\left(K_{13}\left(p_3\nabla p_1^2 - p_1\nabla p_3^2\right) + 2H_{13}p_1p_3\left(p_1 - p_3\right)\right) -$$

$$\frac{\partial g_{13}}{\partial p_1}\frac{\kappa_{Fe_{(s)}\to Fe^{2+}}}{c^{\max}_{Fe_{(s)}}}\left(\exp\left(\frac{(1-\rho)\Lambda_{cor}}{RT}\right) - \frac{c_{Fe^{2+}}}{c^{\max}_{Fe^{2+}}}\exp\left(-\frac{\rho\Lambda_{cor}}{RT}\right)\right) + . \quad (21)$$

$$\frac{L_{Fe_{(s)}\to Fe^{2+}}}{\left(c^{\max}_{Fe_{(s)}}\right)^2}\left(K_{12}\left(p_2\nabla p_1^2 - p_1\nabla p_2^2\right) + 2H_{12}p_1p_2\left(p_1 - p_2\right)\right)$$

Comparing to Eq. (18.a), the addition of the last term on the right-hand side is to mollify the discontinuity crossing the electrode-ID interface following the approach introduced in ref. [42], and the multiplication of $\partial g_{13}/\partial p_1$ to the second term is to ensure that the reaction only occurs at the electrode-electrolyte interface. Following Kundin *et al.* [42], the function g_{ij} is expressed as:

$$g_{ij} = \left[\frac{h\left(p_i\right)}{\sum_k^n h\left(p_k\right)}\right]\left[\frac{h\left(p_j\right)}{\sum_{k\neq i}^n h\left(p_k\right)}\right]. \quad (22)$$

Similarly, noting that p_2 is the normalized concentration of $Fe(OH)_{2(s)}$, we have $\partial p_2/\partial t \sim r_{Fe(OH)_{2(ppt)}\to Fe(OH)_{2(s)}}\Big/c^{\max}_{Fe(OH)_{2(s)}}$. The governing equation for p_2 is then:

$$\frac{\partial p_2}{\partial t} = \frac{L_{Fe(OH)_{2(ppt)}\to Fe(OH)_{2(s)}}}{\left(c^{\max}_{Fe(OH)_{2(s)}}\right)^2}\left(K_{23}\left(p_3\nabla p_2^2 - p_2\nabla p_3^2\right) + 2H_{23}p_2p_3\left(p_2 - p_3\right)\right) +$$

$$\frac{\partial g_{23}}{\partial p_2}\frac{\kappa_{Fe(OH)_{2(ppt)}\to Fe(OH)_{2(s)}}}{c^{\max}_{Fe(OH)_{2(s)}}}\left(\left(\frac{c_{Fe(OH)_{2(ppt)}}}{c^{\max}_{Fe(OH)_{2(ppt)}}}\right)\exp\left(\frac{(1-\rho)\Lambda_{dep}}{RT}\right) - \exp\left(-\frac{\rho\Lambda_{dep}}{RT}\right)\right) + . \quad (23)$$

$$\frac{L_{Fe(OH)_{2(ppt)}\to Fe(OH)_{2(s)}}}{\left(c^{\max}_{Fe(OH)_{2(s)}}\right)^2}\left(K_{21}\left(p_1\nabla p_2^2 - p_2\nabla p_1^2\right) + 2H_{21}p_2p_1\left(p_2 - p_1\right)\right)$$

The variation in concentrations in an electrolyte is governed by the Nernst-Planck

equation:

$$\frac{\partial c_*}{\partial t}=\nabla\left(D_*\nabla c_* + n_* \frac{D_* F c_*}{RT}\nabla\varphi \right)+r_* \quad , \tag{24.a}$$

$$D_* = h\left(p_1\right)D_*^{M} + h\left(p_2\right)D_*^{IDs} + h\left(p_3\right)D_*^{L}, \tag{24.b}$$

where D_* is the diffusion coefficient of the chemical specie $*$, and the superscript "*M*", "*IDs*", "*L*" represent the metallic electrode, IDs, and electrolyte phases, respectively. In Eq. (24.a), the first term on the right-hand side describes the diffusion driven by concentration gradient and electric potential; the second is the source or sink due to reactions (See Appendix C).

The electric field is governed by the Poisson equation, expressed as:

$$\nabla\left(-\varepsilon\nabla\varphi\right)=\sum\frac{n_* F\partial c_*}{\partial t}\ \left(*=\left(c_{Na^+},c_{Cl^-},c_{H^+},c_{OH^-},c_{Fe^{2+}},c_{e^-}\right)\right), \tag{25.a}$$

where ε is the electric conductivity, expressed as:

$$\varepsilon = h\left(p_1\right)\varepsilon^{M} + h\left(p_2\right)\varepsilon^{IDs} + h\left(p_3\right)\varepsilon^{L}. \tag{25.b}$$

The displacement field is governed by equilibrium equation, expressed as:

$$\mathrm{div}\left[h\left(p_1\right)\mathbf{D}^{\mathrm{e}}\left(\frac{1}{2}\left(\frac{\partial d_i}{\partial x_j}+\frac{\partial d_j}{\partial x_i}\right)\right)\right]=0\,. \tag{26}$$

3. Numerical results and discussion

Fig. 2

To implement above governing equations, let us consider, for simplicity, a 2D scenario as shown in Fig. 2. The numerical model consists of a metallic electrode and an electrolyte of the dimensions 80 μm × 40 μm and 80 μm × 500 μm, respectively. Between them a 0.2-μm thick

passive film is assumed, which has a breach of the width a = 4 μm. Beneath the breach, an initial semi-ellipsoid pit is assumed with the semi-major and semi-minor axes a = 4 μm and b = 0 ~ 4 μm, respectively. Owing to symmetry, only half of the model as shown in Fig. 2 was solved.

The initial phase order parameter, **p**, is set to be $\mathbf{p} = \{p_1 = 1, p_2 = 0, p_3 = 0\}$ in the electrode, $\mathbf{p} = \{p_1 = 0, p_2 = 1, p_3 = 0\}$ in the ID, and $\mathbf{p} = \{p_1 = 0, p_2 = 0, p_3 = 1\}$ in the electrolyte. The zero-flux conditions for the phase order parameter, **p**, are applied to all sides of the model domain. The initial concentrations in the electrolyte and the far field (top boundary) are set as $\mathbf{c} = \{c_{Na^+} = 0.2 \text{ mol L}^{-1},\ c_{Cl^-} = 0.2 \text{ mol L}^{-1},\ c_{H^+} = 10^{-7} \text{ mol L}^{-1},\ c_{OH^-} = 10^{-7} \text{ mol L}^{-1},\ c_{O_2} = 10^{-5} \text{ mol L}^{-1}\}$ simulating the ocean environment. For other sides, zero-flux conditions of diffusible substances are applied. The electrical potential at the top of the electrolyte is set as $\varphi_L = 0$. At the bottom of the metal, the zero-flux boundary and the Dirichlet boundary with uniform electric potential, φ_M, are, respectively, applied to simulate the spontaneous Galvanic-cell corrosion and the corrosion under the applied electric field. For mechanical boundary conditions, the top of the metal is unconstrained; the bottom and right are constrained along their normal direction; and a tensile traction is applied to the left boundary. The passive film is assumed to be a zero-flux boundary for the phase order parameter, **p**, ion concentrations, **c**, and electrical field, **φ**. However, the transport of electrons through the passive film is assumed because a passive film usually contains some electroconductive components (e.g., Fe_3O_4). This assumption is also necessary in the present study as it allows the cathodic reactions at the

surface of IDs (Eqs. (1.e) and (1.f)). The temperature is set as 20 °C in simulation. The parameters used in simulation are listed in Table 1. The COMSOL Multiphysics® modeling software [55] is employed for the solution of the proposed multi-PF model. To guarantee the convergence of the solution and have a reasonable computational efficiency, the simulation domain was divided into two parts, as shown in Fig. D1 (see Appendix D). Part I contains both the metallic part and the electrolyte, wherein a uniform square mesh with the element size of 0.2 μm (i.e., 1/5 of the interface thickness) was adopted because the migrations of interfaces must be accurately described in this region. Part II is the far-field electrolyte, the uniform square mesh with the larger size of 2 μm was adopted to solve ion diffusions. Triangle elements with the maximum size of 2 μm were used to mesh the transition region between part I and part II. The non-linear governing equations were solved by using the Newton-Raphson method in COMSOL, in which the time step was automatically refined, if necessary, to ensure the convergence of a solution step. In our simulations, the initial and maximum time steps were 0.001 and 0.05 s, respectively, which have been sufficiently small to ensure a stable solution. Fig. D2 shows the variation of time step in a simulation determined by COMSOL, showing that the time step quickly increased from 0.001 to 0.05 s in the first few steps and then remained at 0.05 s, illustrating the stability of the nonlinear solution.

Table 1

3.1. Evolutions of pit and local environment

Fig. 3

The typical results of simulated local corrosion are shown in Fig. 3. Because the corrosion rates are almost identical along the interface between the electrolyte and the metal, the initial flat breach of the passive film evolves gradually to a semi-circular corrosion pit, as shown in Fig. 3(a), which has also been revealed in previous studies [26 – 27, 32 – 33]. Associated with the enlargement of the pit, the ID also grows. Because the diffusion pathway for corrosion products is constrained by the passive film, the deposition rate of $Fe(OH)_2$ are higher near the corrosion pit, leading to the result that the ID blocks the pit and forms a occluded cell zone. In Laycock *et al.*'s [56] and Almuaili's [57] experiments, it was found that corrosion products suspended over the surface of pit and floating in the electrolyte. These IDs connected and formed a porous cover, known as the lacy cover [56, 57]. While we only deal with one ID in the present numerically study, we would like to remark that a lacy cover can also be reproduced if the random nucleation of IDs is involved in our model, which can be achieved by adding noise terms into governing equations.

Once the occluded cell zone forms, the significant increase in acidity can be observed, as shown in Fig. 3(b). This evolution has been the fundamental concept in occluded cell corrosion as stated by Brown [58], that is the acidity is caused by the hydrolysis of one or more components of salt ($FeCl_2$ in the present work) and it persists because of the restricted interchange between the occluded cell zone and the bulk environment. The significant decrease

in pH have also been experimentally reported by Loete *et al.* [59]. In their experiment, an artificial occluded corrosion cell with the size of a few hundred micrometers is employed and a device similar to total internal reflection fluorescence microscopy was developed to image the pH profiles in a corrosion cell. We also note that the gradual decrease in pH have also been experimentally observed in an artificial crevice corrosion by Bogar *et al.* [60] and Wolfe *et al.* [61]. With the simulation, the rapid accumulation of Cl^- anions in the occluded cell zone can be observed, as shown in Fig. 3(c), which is owing to the hydrolysis of $FeCl_2$ and the transport of Cl^- anions from outside to neutralize the positive charges of Fe^{2+} and H^+. Note that Cl^- has an autocatalytic effect on the formation and hydrolysis of $FeCl_2$, as shown in Eqs. (1.b and 1.c). This causes the rapid increase in the acidity in the occluded cell zone.

The formation of occluded cell zone also results in a sudden change in the local electric field, as shown in Fig. 3(d). We plot the electric potentials in the metallic electrode, φ_M, and the electrolyte in the pit, φ_L, in Fig. 4(a). It is observed that the variation of φ_M exhibits three stages, that is, it first decreases to a negative potential with a reduced decreasing rate, then quickly increases, and finally levels off at a positive value. For φ_L, it always increases with time, which may also be divided into slow-fast-slow three stages, as shown in Fig. 4(a). It is noted that the electric potential difference at electrode-electrolyte interface, $\varphi_M - \varphi_L$, remains negative, as shown in Fig. 4(a).

Fig. 4

The variations in the localized electric field is certainly the consequence of the change in

the local chemical environment and the formation of the occluded cell zone. During corrosion, anodic dissolution releases Fe^{2+} anions into the electrolyte with electrons flowing into IDs. The former reacts with Cl^-, OH^+ to form $FeCl_2$ and $Fe(OH)_2$ in electrolyte, and the latter reacts with H^+ and O_2 at the surface of IDs, named cathodic semi-reaction. At the beginning, the opening of the pit allows chemical substances, such as Cl^-, H^+, $FeCl_2$, to escape from the corrosion pit into the outside environment; therefore, the reactions in the electrolyte are homogenous and the cathodic semi-reaction at the surface of IDs are very weak. Consequently, the negative charges producing from anodic dissolution cannot be fully neutralized by cathodic semi-reaction and accumulate in the metallic electrode, leading to the rapid decrease in φ_M. Meanwhile, as the chemical environment remains almost unchanged, the electric potential in the electrolyte varies very slowly. Consequently, the electrode-electrolyte potential difference $\varphi_M - \varphi_L$, being negative, becomes increasingly larger in magnitude, as shown in Fig. 4(a), which is the characteristic of the early-stage corrosion. When the occluded cell forms, the rapid increase in acidity accelerates the cathodic semi-reaction, which results in a remarkable decrease in the negative charge in the metallic electrode. Meanwhile, the enhanced cathodic semi-reaction also promotes the anodic semi-reaction, producing more Fe^{2+} and H^+ in the local environment and resulting in the rapid increase in the positive charge in the electrolyte. Consequently, the combination of the decrease in negative charge in metallic electrode and the increase in positive charge in electrolyte results in the increase in the electric potential for both of electrode and electrolyte, which leads to the reduction of electric potential difference $\varphi_M -$

φ_L as shown in Fig. 4(a).

Equation (17.c) indicates that if mechanical stress does not present, the driving force of pitting corrosion is dictated by the potential difference, $\varphi_M - \varphi_L$. Therefore, the increasing negativity in $\varphi_M - \varphi_L$ in the early stage leads to the decrease in the driving force of pitting, which suppresses the anodic dissolution and slows down the pitting. After the occluded cell forms, the rapid increase in $\varphi_M - \varphi_L$ results in the fast increase in the corrosion driving force and accelerates the pitting. Consequently, a concave-to-convex (convex-upward-to-concave-downward) transition in the evolution of the pitting depth is expected, as shown in Fig. 4(b), which has also been observed in other numerical studies [21].

With the numerical model, we can further study the impact of aggressive chemical substances, such as Cl^- and H^+, on the localized corrosion. The initial and boundary concentrations of Cl^- may be varied from 0.1 mol L^{-1} to 0.3 mol L^{-1} to simulate diluted saltwater environments, and the concentrations of H^+ is varied from 10^{-7} mol L^{-1} to 10^{-2} mol L^{-1} to simulate the variation from neutral to acid environments. The neutralization of the chemical environment is assumed considering the existence of Na^+ and other cations. To have a systematic comparison, we consider the following four cases:

Case I： $c_{Cl^-} = 0.1$ mol L^{-1}, $c_{H^+} = 10^{-7}$ mol L^{-1}

Case II: $c_{Cl^-} = 0.2$ mol L^{-1}, $c_{H^+} = 10^{-7}$ mol L^{-1}

Case III: $c_{Cl^-} = 0.3$ mol L^{-1}, $c_{H^+} = 10^{-7}$ mol L^{-1}

Case IV: $c_{Cl^-} = 0.2$ mol L^{-1}, $c_{H^+} = 10^{-2}$ mol L^{-1}

Fig. 5

Fig. 5(a) shows the variation of pitting depth with corrosion time for the four cases. In the neutral electrolyte with a low Cl^- concentration, the reactions are homogeneous in the duration of about 300 s, resulting in the gradual reduction in the pit growth rate. However, the further increase in the corrosion time still leads the formation of the occluded cell, resulting in the rapid increase in acidity and the accelerated pit growth rate. The black curves in Figs. 5(a – f) illustrate the concave-to-convex transition in the growth of the pit and the associated remarkable change in the chemical environment and electric field. The increase in Cl^- concentration (Case II) leads to a faster formation of the occluded cell, as indicated by red curves in Figs. 5(a – f), which is the scenario described in Section 3.1. When the chemical environment is more aggressive with the increase in the concentrations of Cl^- and H^+, as exemplified by cases III and IV, the formation of occluded cell is further promoted. In these cases, the concave-to-convex transition in the growth of pit become less obvious because the occluded cell forms at a very early stage. Consequently, although the changes in the chemical environment and electric field are still significant, the growth of the pit becomes approximately linear, because the change in the driving force, $\varphi_M - \varphi_L$, is less significant, as shown by the blue and green curves in Figs. 5(a – f)).

For the purpose of comparison, the corrosion simulation without IDs are also conducted. Note that ID is the cathode. Without ID, we suppose that the metallic component is electronically grounded to direct the flow of electrons, i.e., the Dirichlet boundary conditions

with zero electric potential, $\varphi_M = 0$, and zero concentration of electrons, $c_{e^-} = 0$, are applied at the bottom of metallic electrode. Also, the cathodic reactions, i.e., Eqs. (1.e ~ 1.g), are not involved in the solution.

Fig. 6(a – d) compares the evolutions of Cl^- concentration, pH value at the bottom of the pit, electrode-electrolyte interfacial potential difference, $\varphi_M - \varphi_L$, and pitting depth, respectively, for the cases with and without IDs. It is noted that the variations of Cl^- concentration and pH value are much gentler in the case without IDs than those with IDs (Fig. 6(a, b)), because the diffusions through the open pit without IDs are much easier. Without IDs, the electrode is grounded and the increase in the electric potential in the electrolyte is mainly caused by the accumulation of Fe^{2+} cations. Therefore, $\varphi_M - \varphi_L$ decreases slower that that does with IDs, as shown in Fig. 6(c), leading to the higher pit growth rate than that with IDs, as shown in Fig. 6(d).

Fig. 6

3.2. Effect of mechanical loading

Metallic components are usually subjected mechanical loading, leading to a mechano-chemical coupled corrosion process. To investigate a simple coupling effect, let us consider the scenario that the metallic part in the simulation model is transversely pulled In the region with a breakdown of the passive film, the initial breach is either flat or semi-ellipsoidal (see Fig. 2).

Fig. 7

Figs. 7(a) and (b) show the evolution of the pit morphology when the surface tractions are 100 and 200 MPa (elastic load), respectively, and the concentration in electrolyte is $c_{Cl^-} = 0.2$ mol L^{-1}, $c_{H^+} = 10^{-7}$ mol L^{-1}. While the initial breaches are both flat, the region of stress concentration differs due to the difference in stress magnitude. Under a small tensile traction (e.g., 100 MPa), the initial flat breach turns into a semi-circular pit with an increasing radius, as shown in Fig. 7(a). When the applied tension is larger, the initial flat breach develops into a "W"-shaped pit with corners of stress concentration. It is because that during corrosion, the initial flat corroding surface would firstly develop into a semi-ellipsoid pit with a corner (see the pitting corrosion at 10s in Fig. 7(b)), which results in the stress concentration at the corner rather than the bottom of the pit. Such a stress concentration accelerates the localized corrosion rate, finally resulting in an inhomogeneous metallic dissolution rate and the "W"-shaped pitting, as shown in Fig. 7(b). Note that if the initial pit is already semi-circular, as shown in Fig. 7(c), the stress concentration region remains at the tip, leading to a spear-shaped pit, which has also been observed in our previous study [32].

Fig. 8

Let us further consider two kinds of electrolyte, which are less aggressive ($c_{Cl^-} = 0.1$ mol L^{-1}, $c_{H^+} = 10^{-7}$ mol L^{-1}) and more aggressive ($c_{Cl^-} = 0.3$ mol L^{-1}, $c_{H^+} = 10^{-3}$ mol L^{-1}) than that studied in Fig. 8. Immersing in these two electrolytes, the effect of mechanical stress is more distinct. If the metallic component has an initial flat breach of $a = 4$ μm and $b = 0$ μm and is

under a uniaxial tension of F_x = 250 MPa, Fig. 8(a) shows clearly that the effect of stress is very significant when the chemical environment is aggressive. Note that the applied stress leads to an upturn of the pitting depth (the green curve in Fig. 8(a)) owing to the concentrated stresses at the tip of the pit, as shown in Fig. 8(b). the concentrated stresses accelerate local corrosion, causing in turn the further increase in local stresses. We also note that the initial flat breach could develop into a W-shaped pit with two symmetric corners of stress concentration, as also shown in Fig. 7(b), because the largest curvature occurs near the left/right end of the flat pit during the early development of the pit (i.e., the region at the line of symmetry remains flat). With a large external loading, the stress concentration at the position of largest curvature can accelerate local metallic dissolution rate, resulting in the W-shaped pit, as shown in Fig. 8(b). Such an autocatalysis leads to a rapid stress-corrosion cracking (SCC), which is the most dangerous in application.

3.3 Effect of external electric field

Cathodic protection is the most often employed to resist corrosion, which can be achieved by connecting the metallic components under protection to a more active sacrificing metal. In a power plant, the metallic component may be electrically connected to the negative pole of an external power supply, which maintains a constant electric potential in the metallic component. In the following, the effect of external electric field on pitting corrosion is studied. Shown in Figs. 9(a, b) are the cases that the electric potentials applied (φ_{ap}) to the metallic part

1 are -20 and -50 mV respectively with the chemical environment referring to seawater (c_{Cl^-} =
2 0.2 mol L^{-1}, $c_{H^+} = 10^{-7}$ mol L^{-1}). When the applied electric potential is small, φ_{ap} = -20 mV,
3 φ_L increases with time (Fig. 9(a)); when the applied potential is large, φ_{ap} = -50 mV, φ_L remains
4 almost unchanged (Fig. 9(b)). The comparison of these two scenarios indicates that the applied
5 potential must be larger than a critical magnitude to achieve a strong protection. If the applied
6 electric potential is small, the weak cathodic polarization of metallic electrode still brings
7 about a rapid metallic dissolution, leading to the accumulation of Fe^{2+} in the local environment
8 and the increase in φ_L, the growth of IDs, and finally the formation of occluded cell. With a
9 sufficiently large φ_{ap}, the metallic dissolution can be significantly suppressed so that the
10 chemical environment inside the corrosion pit remains identical to that outside. Thus, $\varphi_M - \varphi_L$
11 remains constant and the linear increase of pitting depth d_c is expected (the blue and green
12 lines in Fig. 10).
13 It is worth stressing that the corrosion behavior under the applied electric field is markedly
14 different from the spontaneous Galvanic-cell corrosion discussed in previous sections. In the
15 spontaneous Galvanic-cell corrosion process, a concave-to-convex transition in the evolution
16 of the pitting depth is observed after occluded cell formation (the dash line in Fig.10). However,
17 if the cathodic protection is implemented, φ_M becomes a constant (the applied external electric
18 potential) and the increasing potential in the electrolyte, due to the accumulation of Fe^{2+} under
19 a small φ_{ap}, leads only to the decrease in the electric potential difference, $\varphi_M - \varphi_L$, and therefore,
20 the gradual slowdown of pitting. But occluded cell can still form after a long-term corrosion

if φ_{ap} is small, which is shown in the inset of Fig. 10.

Fig. 9

Fig. 10

A stress field tends to promote chemical reaction owing to the increase in free energy and the Gutman's effect [40]. In Fig. 8, it has been shown that a large external loading can lead to the dangerous autocatalytic effect on SCC. To avoid the catastrophe, the applied electric potential should counteract the adverse effect of external loading. For example, Fig. 11 shows how the applied electric potential changes the growth kinetics of the corrosion pit when the applied tensile traction is F_x = 250 MPa. It is noted that when φ_{ap} = -10 mV the upturn of the pitting depth due to stress concentration has been suppressed at least within the simulated 100s. With the further increase in φ_{ap} the mean rate of pitting further decreases. When φ_{ap} = -60 mV, the pitting rate has been reduced by more than one order of magnitude compared with the scenario that the external electric field is not applied (shown in the inset of Fig. 11(a)).

Alternatively, the service lifetime of a metallic component may be assessed based on the yield strength. To avoid the dangerous SCC, the tensile stress, σ_x, at the tip of pit should not be larger than the yield strength. As an example, letting the yield stress be 600MPa (the yield strength of high-strength steels is about 600 ~ 1600 MPa), the critical corrosion time, t_{cr}, is determined when the concentrated σ_x at the tip of the pit reaches this critical magnitude, as shown in the inset of Fig. 11(b). Fig. 11(b) shows t_{cr} versus φ_{ap} for the cases of different F_x, which indicates how the service life increases with the applied electric potential. In

engineering applications, such a plot could be useful for the lifetime management of metallic components used in the ocean or more aggressive environments.

Fig. 11

While a quantitative simulation-experiment comparison would best validate our theoretical mode, the former is still difficult because of the limitation of measurement techniques to characterize an actual occluded-cell corrosion. For example, Wolfe *et al.* [61] performed pH measurements using conventional microelectrodes in an artificial crevice with the size over 200 μm, much larger than an actual crevice. Loete *et al.* [59] developed a device similar to a total internal reflection fluorescence microscopy to image the pH profiles in an artificial corrosion cell, of which the size was also hundreds of micrometers. The measurements in these large cells are essentially to obtain the far-field concentration evolutions of chemical substances rather than those in a localized pit. In addition, with a large opening of an artificial cell, occluded cell cannot form spontaneously through the growth of IDs. Consequently, the existing in-situ experiments with artificial cells are still very different from the actual scenario of pitting which we tried to understand based on the multi-PF model.

Nevertheless, some of our numerical result can be supported by experimental findings at least qualitatively. Also, our result is consistent with other numerical models based on other approaches. For example: our simulations reveal that IDs are suspended over the surface of a pit and floating in the electrolyte, which has been observed by Laycock *et al.* [56] and Almuaili [57] in their experiments; the significant decrease in pH, as shown Fig. 3(b), is the most

important phenomenon resulted from occluded-cell corrosion, as stated by Brown [58], which has been experimentally observed by Loete *et al.* [59], Bogar *et al.* [60] and Wolfe *et al.* [61]; and the concave-to-convex transition in the evolution of the pitting depth, as shown in Fig. 4(b) and Fig. 5(a), has also been unveiled in Vautrin-Ul *et al.*'s numerical studies [21], in which a cellular automata model was proposed to study an occluded-cell corrosion. These qualitive comparison make us believe that the proposed model is correct though the proposed parameters may be more accurately determined through a quantitative simulation-experiment comparison, which could soon be possible with the development of experimental technologies.

4. Conclusions

A new multi-PF model is proposed to study localized corrosion which occurs ubiquitously in an ocean environment. In particular, we argue that the establishment of future ocean power plants requires such a simulation tool to predict the service lifetime of metallic components or achieve the more active corrosion control. The theoretical model deals with the formulations of chemical potential, interfacial energy, electrostatic potential energy, and mechanical strain energy, which amount to the Helmholtz free energy of the system. The anodic dissolution and ID formation are treated in the numerical model, which is the reason that a multi-phase-field model is needed. The electrochemical reactions are formulated based on the generalized Allen-Cahn equation, wherein the reaction rates are expressed in the form of Butler–Volmer function. The complete set of governing equations of the multi-PF model involves further the Nernst-

Planck equation, Poisson equation, and the mechanical equilibrium equation, which can be used to tackle mechano-electrochemical coupling in a corrosion process. The main points derived from the simulation results are as follows:

(1). The numerical model reveals not only a detailed occluded cell corrosion process found in experiments but also clarify the complexity involving the anodic-cathodic reaction coupling, the variations in local electric and stress fields, the transports, hydrolysis, and precipitation of chemical substances, and the resulted morphology evolution.

(2). Based on the multi-PF model, the autocatalytic effect resulting from the interplay of the concentrated stresses and the local aggressive chemical environment is predicted. It results in an accelerated increase in the pitting rate; and the concentrated stress leads further to the catastrophic SCC.

(3). The application of an external electric field can significantly reduce the pitting rate and increase the service lifetime of a metallic component, especially when it is stressed. The computational model would be helpful for the lifetime management of metallic components serving in the ocean or other more aggressive environment.

Data Availability

The data that support the findings of this study are available from the corresponding author upon reasonable request.

Code Availability

The code that support the findings of this study are available from the corresponding author upon reasonable request.

Acknowledgments

HHR acknowledges the support of the Early Career Scheme (ECS) of the Hong Kong Research Grants Council (Grant No. 25200515, Account Code F-PP27), the General Research Fund (GRF) (Grant No.: 15213619, Account code: Q73H) of the Hong Kong Research Grants Council. CL acknowledges the support from Natural Science Basic Research Plan in Shaanxi Province of China (No. 2019JQ-123).

Author Contribution

Dr Lin was responsible for the (1) ideation (2) PF model establishment (3) simulation implementation (4) original-writing; Dr Lin, Prof. Ruan was responsible for manuscript (1) discussion (2) writing-review and (3) writing-editing.

Additional Information

Competing Interest: The authors declare no competing interests.

Appendix A

For the anodic corrosion (Eq. (1.a)) at the metallic electrode-electrolyte interface, the chemical potential of the reactant can be derived according to Eqs. (12.a), (14) and (15), which reads:

$$\mu^{ini}_{Fe_{(s)}\to Fe^{2+}} = \left.\frac{\delta F}{\delta c_{Fe_{(s)}}}\right|_{M/L} = \frac{\delta\int_{\Omega}\left(\frac{K_{13}}{2}\left|p_3\nabla p_1 - p_1\nabla p_3\right|^2 + H_{13}p_1^2p_3^2 + f_{mech}\right)d\omega}{c^{\max}_{Fe_{(s)}}\delta p_1} = RT\ln a^{R}_{Fe_{(s)}\to Fe^{2+}} + \mu^{ex}_{Fe_{(s)}}, \tag{A1}$$

where *M/L* denotes that the anodic dissolution only takes place at the metallic electrode-electrolyte interface. The activity of the reaction, $a^{R}_{Fe_{(s)}\to Fe^{2+}}$, and the excess chemical potential, $\mu^{ex}_{Fe_{(s)}}$, are, respectively, expressed as:

$$a^{R}_{Fe_{(s)}\to Fe^{2+}} = \exp\left(\frac{\mu^{\text{int}}_{13}}{RT}\right) = \exp\left(-\frac{K_{13}\left(p_3\nabla p_1^2 - p_1\nabla p_3^2\right) + 2H_{13}p_1p_3\left(p_1 - p_3\right)}{RTc^{\max}_{Fe_{(s)}}}\right), \tag{A2}$$

$$\mu^{ex}_{(Fe)_s} = \frac{\partial f_{mech}}{c^{\max}_{Fe_{(s)}}\delta p_1}. \tag{A3}$$

In Eq. (A2), μ^{int}_{13} represents the chemical potential resulting from the electrode-electrolyte interfacial energy. Eq. (A3) indicates that the excess chemical potential origins from the mechanical deformation of a load-bearing metallic electrode. Referring to the linear relation between free energy and the pressure *P*, Gutman [40] suggested the additional term in chemical potential as $\Delta\mu \approx V_m\Delta P$, where V_{m} is the molar volume of a load-bearing solid. Because tension and compression both increases the chemical potential of the solid materials [40], the pressure, *P*, should be the absolute value of the hydrostatic part of a stress tensor, that is

$P = \left| tr\left(\boldsymbol{\sigma}\right) \right| / 3$. Thus, Eq. (A3) is recast as:

$$\mu_{(Fe)_s}^{ex} = \frac{\partial f_{mech}}{c_{Fe_{(s)}}^{\max} \delta p_1} + \frac{V_m}{3} \left| tr\left(\boldsymbol{\sigma}\right) \right|. \tag{A4}$$

Correspondingly, the chemical potential of the product of the anodic corrosion (Eq. (1.a)), can be derived as:

$$\mu_{Fe_{(s)} \to Fe^{2+}}^{fa} = \left(\frac{\delta F}{\delta c_{Fe^{2+}}} + 2\frac{\delta F}{\delta c_{e^-}} \right)\Bigg|_{M/L} = RT \ln a_{Fe^{2+}} + \mu_{Fe^{2+}}^{ex} + 2\mu_{e^-}^{ex}, \tag{A5}$$

where the first term of the right hand-side of Eq. (A5) represents the contribution from the chemical substances concentration, the second and third term represents the contribution from standard chemical potential and electric field, which are expressed as follows:

$$RT \ln a_{Fe^{2+}} = RT \ln\left(c_{Fe^{2+}} / c_{Fe^{2+}}^{\max} \right), \tag{A6}$$

$$\mu_{Fe^{2+}}^{ex} + 2\mu_{e^-}^{ex} = \mu_{Fe^{2+}}^{0} - 2F\left(\varphi_M - \varphi_L\right). \tag{A7}$$

The chemical potential in the transition state is expressed as:

$$\begin{aligned} \mu_{Fe_{(s)} \to Fe^{2+}}^{ts} &= RT \ln\left(a_{Fe_{(s)} \to Fe^{2+}}^{ts} \right) + \\ &\rho\left(\frac{\partial f_{mech}}{c_{Fe_{(s)}}^{\max} \delta p_1} + \frac{V_m}{3} \left| tr\left(\sigma\right) \right| \right) + \left(1-\rho\right)\left(\mu_{Fe^{2+}}^{0} - 2F\left(\varphi_M - \varphi_L\right) \right) \end{aligned}, \tag{A8}$$

Substituting Eqs. (A1 ~ A8) into Eq. (11) leads to the expression of the reaction rate given in Eqs. (16) and (17).

Appendix B

For the reaction $Fe_{(s)} \rightarrow Fe^{2+} + e^-$, the electric potential difference at the electrode-electrolyte interface under an electrochemical equilibrium can be derived as:

$$\Delta\varphi_{eq} = \left(\varphi_M - \varphi_L\right)_{eq} = \frac{\mu^0_{Fe^{2+}}}{2F} + \frac{RT}{2F}\ln\left(\frac{c_{Fe^{2+}}}{c^{\max}_{Fe^{2+}}}\right) - \frac{\mu^{\text{int}}_{13}}{2F} - \frac{V_m\left|tr\left(\sigma\right)\right|}{6F} - \frac{\partial f_{mech}}{2Fc^{\max}_{Fe_{(s)}}\partial p_1}. \quad \text{(B1)}$$

The electrochemical reaction takes place under the overpotential, η, defined as:

$$\eta = \Delta\varphi - \Delta\varphi_{eq} = \Delta\varphi - \frac{\mu^0_{Fe^{2+}}}{2F} - \frac{RT}{2F}\ln\left(\frac{c_{Fe^{2+}}}{c^{\max}_{Fe^{2+}}}\right) + \frac{\mu^{\text{int}}_{13}}{2F} + \frac{V_m\left|tr\left(\sigma\right)\right|}{6F} + \frac{\partial f_{mech}}{2Fc^{\max}_{Fe_{(s)}}\partial p_1}. \quad \text{(B2)}$$

Subsequently, the reaction rate can also be expressed in the form of the generalized BV equation by substituting Eq. (A2) into Eq. (21.a) as:

$$r_{Fe_{(s)}\to Fe^{2+}} = \kappa_{Fe_{(s)}\to Fe^{2+}}\left(\frac{c_{Fe^{2+}}}{c^{\max}_{Fe^{2+}}}\right)^{1-\rho}\exp\left(\frac{\rho\mu^{\text{int}}_{13}}{RT}\right)\left(\exp\left(\frac{2F\left(1-\rho\right)\eta}{RT}\right) - \exp\left(-\frac{2F\rho\eta}{RT}\right)\right). \quad \text{(B3)}$$

Appendix C

The expression of homogeneous reaction in electrolyte (Eqs. (1.b ~ 1.f)), are listed in Table C1:

Table C1

In table C1, $\vec{k}$ and $\overleftarrow{k}$ are the forward and backward reaction rate coefficients, respectively; K_{eq} is the chemical equilibrium constant in the form of $K_{eq} = \log\left(\vec{k}/\overleftarrow{k}\right)$; $c_{H_2O} =$ 1000 mol m^{-3} [51]. According to reaction formula (Eqs. (1.a ~ 1.g)), the set of sources or sinks for the concentration of chemical substances, r_*, in Eq. (23), can be expressed as:

$$r_{H^+} = r_{H_2O\to H^+ + OH^-} + 2r_{Fe(Cl)_{2(ppt)}\to Fe(OH)_{2(ppt)}} - r_{H^+\to H_2}, \quad \text{(C1.a)}$$

$$r_{OH^-} = r_{O_2\to OH^-} - 2r_{Fe^{2+}\to Fe(OH)_{2(ppt)}}, \quad \text{(C1.b)}$$

$$r_{Cl^-} = 2r_{FeCl_{2(ppt)}\to Fe(OH)_{2(ppt)}} - 2r_{Fe^{2+}\to FeCl_{2(ppt)}}, \quad \text{(C1.c)}$$

$$r_{Fe^{2+}} = r_{Fe_{(s)}\to Fe^{2+}} - r_{Fe^{2+}\to Fe(OH)_{2(ppt)}} - r_{Fe^{2+}\to FeCl_{2(ppt)}}, \quad \text{(C1.d)}$$

$$r_{FeCl_{2(ppt)}} = r_{Fe^{2+}\rightarrow FeCl_{2(ppt)}} - r_{FeCl_{2(ppt)}\rightarrow Fe(OH)_{2(ppt)}}, \quad \text{(C1.e)}$$

$$r_{Fe(OH)_{2(ppt)}} = r_{FeCl_{2(ppt)}\rightarrow Fe(OH)_{2(ppt)}} + r_{Fe^{2+}\rightarrow Fe(OH)_{2(ppt)}} - r_{Fe(OH)_{2(ppt)}\rightarrow Fe(OH)_{2(s)}}, \quad \text{(C1.f)}$$

$$r_{O_2} = -r_{O_2\rightarrow OH^-}, \quad \text{(C1.g)}$$

$$r_{e^-} = 2r_{Fe_{(s)}\rightarrow Fe^{2+}} - 4r_{O_2\rightarrow OH^-} - r_{H^+\rightarrow H_2}, \quad \text{(C1.h)}$$

The diffusion coefficient of the chemical substances, participating the reactions (Eqs. (1.a ~ 1.g)), are listed in Table C2.

Table C2

The ID is considered as a porous media. Therefore, the diffusion coefficient of chemical substances in the IDs are expressed based on the Bruggeman relation [62] as:

$$D_*^{IDs} = \chi^{1.5} D_*^L \quad \left(* = Na^+, Cl^-, H^+, OH^-, Fe^{2+}, FeCl_{2(ppt)}, Fe\left(OH\right)_{2(ppt)}, O_2\right). \quad \text{(C2)}$$

where χ is the porosity of IDs. For the electron transport in IDs, the Diffusion coefficient is set as $D_{e^-}^{IDs} = 10^{-6} D_{e^-}^{M}$. Note that electrons are assumed to transport in IDs and passive film, due to the fact that the compositions of IDs and passive film are usually complex with some electroconductive components, for example Fe_3O_4.

Appendix D

The molar mass and density of $Fe(OH)_2$ are $m_{Fe(OH)_2}$ = 90 g mol^{-1} and $\rho_{Fe(OH)_2}$ = 4 g cm^{-3}, respectively. Thus, the maximum molar concentration of the ID, $Fe(OH)_2$, is $c_{Fe(OH)_2}^{\max} = \rho_{Fe(OH)_2} / m_{Fe(OH)_2}$ = 42 mol L^{-1}.

The equilibrium electric potential of the anodic dissolution of iron is -0.6 V [54]. Thus,

the reference chemical potential, $\mu^0_{Fe^{2+}}$ is about -100 kJ mol^{-1} based on Eq. (B1) by omitting the effect of concentration and stress.

An interfacial reaction can be treated as phase transformation in a phase-field model. Herein, we shall deal with the andic dissolution (Eq. 21) and the IDs formation (Eq. 22). The 1D analytical solutions for the velocity of phase boundary migration can be obtained under the steady state conditions [32], i.e., the elemental concentration, electric potential, and elastic energy no longer change with time, which are expressed as:

$$v_{Fe_{(s)}\to Fe^{2+}} = \kappa_{Fe_{(s)}\to Fe^{2+}}\zeta_{13}\left(\exp\left(\frac{(1-\rho)\Lambda_{cor}}{RT}\right)-\frac{c_{Fe^{2+}}}{c^{\max}_{Fe^{2+}}}\exp\left(-\frac{\rho\Lambda_{cor}}{RT}\right)\right), \tag{D1}$$

$$v_{Fe(OH)_{2(ppt)}\to Fe(OH)_{2(s)}} = \kappa_{Fe(OH)_{2(ppt)}\to Fe(OH)_{2(s)}}\zeta_{23}\left(\left(\frac{c_{Fe(OH)_{2(ppt)}}}{c^{\max}_{Fe(OH)_{2(ppt)}}}\right)\exp\left(\frac{(1-\rho)\Lambda_{dep}}{RT}\right)-\exp\left(-\frac{\rho\Lambda_{dep}}{RT}\right)\right), \tag{D2}$$

where v is the velocity of phase boundary migration.

If the impacts of stress and electric field are negligible, the 1D velocity, $v_{Fe_{(s)}\to Fe^{2+}}$ and $v_{Fe(OH)_{2(ppt)}\to Fe(OH)_{2(s)}}$ can be rewritten as:

$$v_{Fe_{(s)}\to Fe^{2+}} = \kappa_{Fe_{(s)}\to Fe^{2+}}\zeta_{13}\left(\exp\left(-\frac{(1-\rho)\mu^0_{Fe^{2+}}}{RT}\right)-\frac{c_{Fe^{2+}}}{c^{\max}_{Fe^{2+}}}\exp\left(\frac{\rho\mu^0_{Fe^{2+}}}{RT}\right)\right), \tag{D3}$$

$$v_{Fe(OH)_{2(ppt)}\to Fe(OH)_{2(s)}} = \kappa_{Fe(OH)_{2(ppt)}\to Fe(OH)_{2(s)}}\zeta_{23}\left(\left(\frac{c_{Fe(OH)_{2(ppt)}}}{c^{\max}_{Fe(OH)_{2(ppt)}}}\right)\exp\left(\frac{(1-\rho)\mu^0_{Fe(OH)_2}}{RT}\right)-\exp\left(-\frac{\rho\mu^0_{Fe(OH)_2}}{RT}\right)\right). \tag{D4}$$

In this work, $v_{Fe_{(s)}\to Fe^{2+}}$ is set as 0.2 μm s^{-1}, which is a realistic value of localized corrosion [63]. For $v_{Fe(OH)_{2(ppt)}\to Fe(OH)_{2(s)}}$, there is not a measured value. Hence, we assume that it is same

as $v_{Fe_{(s)}\to Fe^{2+}}$. These assumptions lead to the determination of the kinetic coefficients $\kappa_{Fe_{(s)}\to Fe^{2+}} \approx \kappa_{Fe(OH)_{2(ppt)}\to Fe(OH)_{2(s)}} \approx 2\times10^{-10}$ s^{-1}, with $\zeta_{13}=\zeta_{23}=1$ μm, $\rho = 0.5$, $-\mu^0_{Fe^{2+}} = \mu^0_{Fe(OH)_2} = 100$ kJ mol^{-1}, $c_{Fe^{2+}} = 0$ and $c_{Fe(OH)_{2(ppt)}} \Big/ c^{\max}_{Fe(OH)_{2(ppt)}} = 1$.

Fig. D1

Fig. D2

Reference

[1] O. Ellabban, H. Abu-Rub, F. Blaabjerg, Renew. Sust. Energ. Rev. 39 (2014) 748–764.

[2] G.S. Bhuyan, World-wide status for harnessing ocean renewable resources, in: Proceedings of the 2010 IEEE power and energy society general meeting, Providence, RI, USA, 2010.

[3] Z.L. Wang, T. Jiang, L. Xu, Toward the blue energy dream by triboelectric nanogenerator networks, Nano Energy 39 (2017) 9–23.

[4] L. Xu, T. Jiang, P. Lin, J. Shao, C. He, W. Zhong, X. Chen, Z.L. Wang, Coupled Triboelectric Nanogenerator Networks for Efficient Water Wave Energy Harvesting, ACS Nano 12 (2018) 1849–1858.

[5] C. Wu, A.C. Wang, W. Ding, H. Guo, Z.L. Wang, Triboelectric Nanogenerator: A Foundation of the Energy for the New Era, Adv. Energy Mater. 9, 1802906 (2019).

[6] Q. Shi, T. He, C. Lee, More than energy harvesting-Combining triboelectric

nanogenerator and flexible electronics technology for enabling novel micro-/nano-systems, Nano Energy 57 (2019) 851–871.

[7] B. Hou, X. Li, X. Ma, C. Du, D. Zhang, M. Zheng, W. Xu, D. Lu, F. Ma, The cost of corrosion in China, Npj Mater. Degrad. 1 (2017) 4.

[8] J.R. Galvele, Pittlng Corrosion, In: Treatise on Materials Science and Technolosy. Vol. 23. Corrosion: Aqueous Processes and Passive Films (J.C. Scully, Ed.), Academic Press, London. (1983) 1−57.

[9] M.G. Alvarez, J.R. Galvele, The mechanism of pitting in high purity iron in NaCl solutions, Corros. Sci., 24 (1984) 27−48.

[10] J.R. Galvele, R.M. Torresi, R.M. Carranza, Passivity breakdown, its relation to pitting and stress-corrosion-cracking processes, Corros. Sci., 31 (1990) 563−571.

[11] E. McCafferty, Calculation of current distribution in circular corrosion cells, Corros. Sci., 16 (1976) 183−190.

[12] J.R. Galvele, Transport processes in passivity breakdown—II. Full hydrolysis of the metal ions, Corros. Sci., 21 (1981) 551−579.

[13] S.M. Sharland, P.W. Tasker, A mathematical model of crevice and pitting corrosion- I. The physical model, Corros. Sci., 28 (1988) 603–620.

[14] O. Guseva, P. Schmutz, T. Suter, O. von Trzebiatowski, Modelling of anodic dissolution of pure aluminum in sodium chloride, Electrochim. Acta 54 (2009) 4514–4524.

[15] K.B. Deshpande, Numerical modeling of micro-galvanic corrosion, Electrochim. Acta 56

(2011) 1737–1745.

[16] J. Cui, F. Yang, T.H. Yang, G.F. Yang, Numerical study of stainless steel pitting process based on the lattice Boltzmann method, Int. J. Electrochem. Sci. 14 (2019) 1529–1545.

[17] S. Sarkar, J.E. Warner, W. Aquino, A numerical framework for the modeling of corrosive dissolution, Corros. Sci. 65 (2012) 502–511.

[18] R. Duddu, Numerical modeling of corrosion pit propagation using the combined extended finite element and level set method, Comput. Mech. 54 (2014) 613–627.

[19] S. Jafarzadeh, Z. Chen, S. Li, F. Bobaru, A peridynamic mechano-chemical damage model for stress-assisted corrosion, Electrochim. Acta 323 (2019) 134795.

[20] S. Jafarzadeh, Z. Chen, J. Zhao, F. Bobaru, Pitting, lacy covers, and pit merger in stainless steel: 3D peridynamic models, Corros. Sci. 150 (2019) 17–31.

[21] C. Vautrin-Ul, H. Mendy, A. Taleb, A. Chaussé, J. Stafiej, J. Badiali, Numerical simulations of spatial heterogeneity formation in metal Corrosion, Corros. Sci. 50 (8) (2008) 2149–2158.

[22] H. Wang, E.-H. Han, Computational simulation of corrosion pit interactions under mechanochemical effects using a cellular automaton/finite element model, Corros. Sci. 103 (2016) 305–311.

[23] O.O. Fatoba, R. Leiva-Garcia, S.V. Lishchuk, N.O. Larrosa, R. Akid, Simulation of stress-assisted localized corrosion using a cellular automaton finite element approach, Corros. Sci. 137 (2018) 83–97.

[24] C. Chuanjie, M. Rujin, C. Airong, P. Zichao, T. Hao, Experimental study and 3D cellular automata simulation of corrosion pits on Q345 steel surface under salt-spray environment, Corros Sci 154 (2019) 80–89.

[25] Z. Xiao, S. Hu, J. Luo, S.Q. Shi, C. Henager, A quantitative phase-field model for crevice corrosion, Comput. Mater. Sci. 149 (2018), 37–48.

[26] T.Q. Ansari, Z. Xiao, S. Hu, Y. Li, J. Luo, S.Q. Shi, Phase-field model of pitting corrosion kinetics in metallic materials, npj Comput. Mater. 38 (2018).

[27] W. Mai, S. Soghrati, R.G. Buchheit, A phase field model for simulating the pitting corrosion, Corros. Sci. 110 (2016) 157–166.

[28] A.F. Chadwick, J.A. Stewart, R.A. Enrique, S. Du, K. Thornton, Numerical modeling of localized corrosion using phase-field and smoothed boundary methods. J. Electrochem. Soc. 165 (2018) C633–C646.

[29] L. Yin, Y. Jin, C. Leygraf, J. Pan, A FEM model for investigation of micro-galvanic corrosion of Al alloys and effects of deposition of corrosion products, Electrochim. Acta 192 (2016) 310–318.

[30] Y. Wang, L. Yin, Y. Jin, J. Pan, C. Leygraf, Numerical simulation of microgalvanic corrosion in al alloys: steric hindrance effect of corrosion product, J. Electrochem. Soc. 164 (2017) C1035–C1043.

[31] W. Mai, S. Soghrati, New phase field model for simulating galvanic and pitting corrosion processes, Electrochim. Acta 260 (2018) 290–304.

[32] C. Lin, H.H. Ruan, S.Q. Shi, Phase field study of mechanico-electrochemical corrosion, Electrochim. Acta 310 (2019) 240–255.

[33] T.Q. Ansari, J. Luo, S.Q. Shi, Modeling the effect of insoluble corrosion products on pitting corrosion kinetics of metals, Npj Mater. Degrad. 3 (2019) 28.

[34] R.K. Ren, S. Zhang, X.L. Pang, K.W. Gao, A novel observation of the interaction between the macroelastic stress and electrochemical corrosion of low carbon steel in 3.5 wt% NaCl solution, Electrochim. Acta 85 (2012) 283–294.

[35] X.H. Wang, X.H. Tang, L.W. Wang, C. Wang, Z.Z. Guo, Corrosion behavior of X80 pipeline steel under coupling effect of stress and stray current, Int. J. Electrochem. Sci. 9 (2014) 4574–4588.

[36] X. Feng, X. Lu, Y. Zuo, N. Zhuang, D. Chen, Electrochemical study the corrosion behaviour of carbon steel in mortars under compressive and tensile stresses, Corros. Sci. 103 (2016) 66–74.

[37] H.Q. Yang, Q. Zhang, S.S. Tu, Y. Wang, Y.M. Li, Y. Huang, Effects of inhomogeneous elastic stress on corrosion behaviour of Q235 steel in 3.5% NaCl solution using a novel multi-channel electrode technique, Corros. Sci. 110 (2016) 1–14.

[38] S.J. Kim, Effect of the elastic tensile load on the electrochemical corrosion behavior and diffusible hydrogen content of ferritic steel in acidic environment, Int. J. Hydrogen Energy 42 (2017) 19367–19375.

[39] X.H. Zhao, Y.R. Feng, S.W. Tang, J.X. Zhang, Electrochemical corrosion behavior of

15Cr-6Ni-2Mo stainless steel with/without stress under the coexistence of CO2 and H2S, Int. J. Electrochem. Sci. 13 (2018) 6296–6309.

[40] E.M. Gutman, Mechanochemistry of solid surfaces, World Scientific, 1994.

[41] S. Sarkar, W. Aquino, Changes in electrodic reaction rates due to elastic stress and stress-induced surface patterns, Electrochim. Acta 111 (2013) 814–822.

[42] J. Kundin, R. Siquieri, H. Emmerich, A quantitative multi-phase-field modeling of the microstructure evolution in a peritectic Al–Ni alloy, Physica D, 243 (2013) 116–127.

[43] K. Ammar, B. Appolaire, G. Cailletaud, F. Feyel, S. Forest, Finite element formulation of a phase field model based on the concept of generalized stresses, Comp. Mater. Sci., 45 (2009) 800–805.

[44] R. Folch, M. Plapp, Quantitative phase-field modeling of two-phase growth, Phys. Rev. E, 72 (2005) 011602.

[45] M.E. Gurtin, E. Fried, L. Anand. The mechanics and thermodynamics of continua. Cambridge: Cambridge University Press; 2010.

[46] S.-L. Wang, R.F. Sekerka, A.A. Wheeler, B.T. Murray, S.R. Coriell, R.J. Braun, G.B. McFadden, Thermodynamically-consistent phase-field models for solidification, Physica D, 69 (1993) 189–200.

[47] N. Birks, G. H. Meier, Introduction to the High Temperature Oxidation of Metals, Cambridge University Press, 2012.

[48] M. Z. Bazant, Theory of Chemical Kinetics and Charge Transfer based on Nonequilibrium

Thermodynamics, Acc. Chem. Res., 46 (2013) 1144–1160.

[49] A.M. Kuznetsov, J. Ulstrup, Electron Transfer in Chemistry and Biology: An Introduction to the Theory, Wiley: Chichester, U.K., 1999.

[50] K.L. Heppner, R.W. Evitts, J. Postlethwaite, Effect of Ionic Interactions on the Initiation of Crevice Corrosion in Passive Metals, J. Electrochem. Soc. 152 (2005) B89–B98.

[51] S. Salleh, Modelling pitting corrosion in carbon steel materials, The University of Manchester 2013.

[52] S. Gavrilov, M. Vankeerberghen, G. Nelissen, J. Deconinck, Finite element calculation of crack propagation in type 304 stainless steel in diluted sulphuric acid solutions, Corros. Sci. 49 (2007) 980–999.

[53] J.C. Walton, G. Cragnolino, S.K. Kalandro, A numerical model of crevice corrosion for passive and active metals, Corros. Sci. 38 (1996) 1–18.

[54] M. Randall, M. Frandsen, The standard electrode potential of iron and the activity coefficient of ferrous chloride, J. Am. Chem. Soc. 54 (1932) 47–54.

[55] COMSOL Multiphysics Users' Guide. Available from: http://www.comsol.com/.

[56] N. Laycock, M.H. Moayed, R. Newman, Metastable pitting and the critical pitting temperature, J. Electrochem. Soc. 145 (1998) 2622–2628.

[57] F. Almuaili, Characterization of 3D Pitting Corrosion Kinetics of Stainless Steel in Chloride Containing Environments, Doctoral dissertation University of Manchester, 2017.

[58] B.F. Brown, Concept of the occluded corrosion cell, Corrosion 26 (8) (1970) 349–350.

[59] F. Loëte, B.Vuillemin, R. Oltra, D. Chaumont, E. Bourillot, Application of total internal reflexion fluorescence microscopy for studying pH changes in an occluded electrochemical cell: Development of a waveguide sensor, Electrochem. Commun., 8 (2006), 1016–1020.

[60] F. D. Bogar and C. T. Fujii, Solution chemistry in crevices on Fe-Cr binary alloys, US Nat. Tech. Inform. Serv., AD Rep. No. 778002/6GA (1974).

[61] R.C. Wolfe, K.G. Weil, B.A. Shaw, H.W. Pickering, Measurement of pH gradients in the crevice corrosion of iron using a palladium hydride microelectrode, J. Electrochem. Soc., 152 (2005), B82–B88.

[62] B. Tjaden, S. J. Cooper, D.J. Brett, D. Kramer, P.R. Shearing, On the origin and application of the Bruggeman correlation for analysing transport phenomena in electrochemical systems, Curr. Opin. Chem. Eng., 12 (2016) 44–51.

[63] P.C. Pistorius, G.T. Burstein, Metastable pitting corrosion of stainless steel and the transition to stability, Philos. Trans. R. Soc. Lond. Ser. A: Phys. Eng. Sci., 341 (1992) 531–559.

Figure caption

Fig. 1 Schematics of occluded cell corrosion.

Fig. 2 The geometry and boundary condition of simulation.

Fig. 3 Evolution of pitting corrosion and local environment, herein (a) describes the dissolution of metallic electrode (p_1 =1), and the formation of IDs ($2p_2$ = 2); (b ~ d) characterizes the evolution of PH, concentration of Cl^-, and electric potential, respectively.

Fig. 4 Evolution of (a) electric potential and (b) pit depth, d_c, with corrosion time.

Fig. 5 Effect of chemical environments on evolutions of (a) pitting depth, (b) concentration of Cl^-, (c) pH value at the bottom of the pit, (d, e) the electric potentials in the electrolyte, the electrode, respectively, and (f) the electrode-electrolyte interfacial electric potential difference, $\varphi_M - \varphi_L$.

Fig. 6 Evolution of (a) concentration of Cl^-, (b) pH value at the bottom of the pit, (c) the electrode-electrolyte interfacial electric potential difference, $\varphi_M - \varphi_L$ and (d) the pitting depth for the corrosion process with and without IDs.

Fig. 7 Evolution of pitting corrosion with stress development for the metallic components with (a, b) an initial flat corroding surface and (c) an initial semi-ellipsoid breach (the semi-major and semi-minor axes being, respectively, $a = b$ = 4 μm), which are under the uniaxial tension, F_x = (a, b) 100 and (c) 200 MPa. The concentrations in electrolyte are c_{Cl^-} = 0.2 mol L-1, $c_{H^+} = 10^{-7}$ mol L^{-1}.

Fig. 8 Comparison of the evolutions of (a) the pitting depth, d_c, and (b) the concentrated normal stress (σ_x) at the tip of pit under different chemical environments (mild and aggressive) and applied stress (0, 250 MPa). In this demonstration, The mild and aggressive chemical environments refer to (c_{Cl^-} = 0.1 mol L^{-1}, c_{H^+} = 10^{-7} mol L^{-1}) and (c_{Cl^-} = 0.3 mol L^{-1}, c_{H^+} = 10^{-3} mol L^{-1}), respectively.

Fig. 9 Contour plots of electric field with time for the metallic component under the applied potential, φ_{ap} = (a) -20 and (b) -50 mV.

Fig. 10 Evolution of depth of corrosion pit under the applied potential, φ_{ap}; the inset shows the occluded cell formation when the applied potential φ_{ap} is -20 mV.

Fig. 11 Effect of applied potential on (a) the variation of the pitting depth when passive film has a flat breach; and (b) the service lifetime t_{cr}. In (a), the aggressive electrolyte of (c_{Cl^-} = 0.3 mol L^{-1}, c_{H^+} = 10^{-3} mol L^{-1}) and the tensile traction of F_x = 250 MPa were considered; and the inset shows the mean rate of pitting, v_{tip}^m, versus φ_{ap}. In (b), t_{cr} is assessed based on the critical stress as shown in the inset; and three cases were simulated: A. F_x = 250 MPa and seawater (c_{Cl^-} = 0.2 mol L^{-1}, c_{H^+} = 10^{-7} mol L^{-1}), B. F_x = 250 MPa and the aggressive electrolyte (c_{Cl^-} = 0.3 mol L^{-1}, c_{H^+} = 10^{-3} mol L^{-1}), and C. F_x = 350 MPa and seawater (c_{Cl^-} = 0.2 mol L^{-1}, c_{H^+} = 10^{-7} mol L^{-1}).

Fig. D1 FE mesh of the geometry used in simulation.

Fig. D2 Convergence curve for the case: c_{Cl^-} = 0.2 mol L^{-1}, c_{H^+} = 10^{-7} mol L^{-1}.

1 **Table**

	Parameter	Value
Interfacial energy density	$S_{12} = S_{13} = S_{23}$	1 J m^{-2} [32]
Interface thickness	$\zeta_{12} = \zeta_{13} = \zeta_{23}$	1 μm [32]
Young's modulus of the metal phase	E	200 GPa
Poisson's ratio of the metal phase	v	0.33
Maximum concentration of metal (Fe)	$c^{\max}_{Fe_{(s)}}$	1.4×10^{2} mol L^{-1} [32]
Maximum concentration of metal ion in electrolyte (Fe^{2+})	$c^{\max}_{Fe^{2+}}$	5.436 mol L^{-1} [32]
Maximum concentration of IDs ($Fe(OH)_2$)	$c^{\max}_{Fe(OH)_{2(s)}}$	4.2×10 mol L^{-1} (See Appendix D)
Coefficients to scale the contributions of the interfacial energy	$L_{Fe_{(s)}\rightarrow Fe^{2+}} = L_{Fe(OH)_{2(ppt)}\rightarrow Fe(OH)_2}$	$10^{-9}/m^3$ J^{-1} s^{-1}
Reference chemical potential of Fe^{2+}	$\mu^{0}_{Fe^{2+}}$	-100 kJ mol^{-1} (See Appendix D)
Reference chemical potential of	$\mu^{0}_{Fe(OH)_2}$	100 kJ mol^{-1}

$Fe(OH)_2$		
Coefficient to scale the contributions of anodic dissolution kinetics	$\kappa_{Fe_{(s)} \to Fe^{2+}}$	2×10^{-10} s^{-1} (See Appendix D)
Coefficient to scale the contributions of ID formation kinetics	$\kappa_{Fe(OH)_{2(ppt)} \to Fe(OH)_2}$	2×10^{-10} s^{-1} (See Appendix D)
Asymmetry factor	ρ	0.5 [32]
Electric conductivity of electrolyte	ε^L	1 S m^{-1} [32]
Electric conductivity of IDs	ε^{IDs}	1 S m^{-1} [32]
Electric conductivity of metal (M)	ε^S	10^7 S m^{-1} [32]
Ideal gas constant	R	8.314 J mol^{-1} K^{-1}
Faraday's constant	F	96485 C mol^{-1}
Porosity of IDs	χ	0.05

Table 1 Parameters used in simulation

Reaction formula	Reaction rate expression	K_{eq}	$\vec{k}$
$H_2O \rightleftharpoons H^+ + OH^-$	$r_{H_2O \to H^+ + OH^-} = \vec{k}_{H_2O \to H^+ + OH^-} - \overleftarrow{k}_{H_2O \to H^+ + OH^-} c_{H^+} c_{OH^-}$	14 [50]	1 mol m^{-3} s^{-1}
$Fe^{2+} + 2OH^- \to Fe(OH)_{2(ppt)}$	$r_{Fe^{2+} \to Fe(OH)_{2(ppt)}} = \vec{k}_{Fe^{2+} \to Fe(OH)_{2(ppt)}} c_{Fe^{2+}} c^2_{OH^-}$	-	10^5 m^6 mol^{-2} s^{-1}
$Fe^{2+} + 2Cl^- \rightleftharpoons FeCl_{2(ppt)}$	$r_{Fe^{2+} \to FeCl_{2(ppt)}} = \vec{k}_{Fe^{2+} \to FeCl_{2(ppt)}} c_{Fe^{2+}} c^2_{Cl^-} - \overleftarrow{k}_{Fe^{2+} \to FeCl_{2(ppt)}} c_{FeCl_{2(ppt)}}$	-2 [50]	10^{-3} m^6 mol^{-2} s^{-1}
$FeCl_{2(ppt)} + 2H_2O \rightleftharpoons Fe(OH)_{2(ppt)} + 2Cl^- + 2H^+$	$r_{FeCl_{2(ppt)} \to Fe(OH)_{2(ppt)}} = \vec{k}_{FeCl_{2(ppt)} \to Fe(OH)_{2(ppt)}} c_{FeCl_{2(ppt)}} c^2_{H_2O} - \overleftarrow{k}_{FeCl_{2(ppt)} \to Fe(OH)_{2(ppt)}} c^2_{Cl^-} c^2_{H^+}$	-0.4 [51]	10^{-5} m^6 mol^{-2} s^{-1}
$e^- + H^+ \to H_2/2$	$r_{H^+ \to H_2} = \vec{k}_{H^+ \to H_2} c_{e^-} c_{H^+}$	-	10^5 m^3 mol^{-1} s^{-1}
$e^- + 4O_2 + 2H_2O \to 4OH^-$	$r_{O_2 \to OH^-} = \vec{k}_{O_2 \to OH^-} \left(c_{e^-}\right)^4 c_{O_2}$	-	10^5 m^{12} mol^{-4} s^{-1}

Table C1 Reaction rate formula.

Chemical substances	Diffusion coefficient in electrolyte D^L (m^2 s^{-1})	Diffusion coefficient in metal D^M (m^2 s^{-1})
H^+	9.31×10^{-9} [52]	-
OH^-	5.22×10^{-9} [52]	-
Fe^{2+}	1×10^{-9} [52]	-
Na^+	1.3×10^{-9} [53]	-
Cl^-	2×10^{-9} [53]	-
$Fe(OH)_2$	1×10^{-9} [53]	-
$FeCl_2$	1×10^{-9} [53]	-
O_2	2.04×10^{-9} [52]	-

Table C2 Diffusion coefficients of chemical substances.

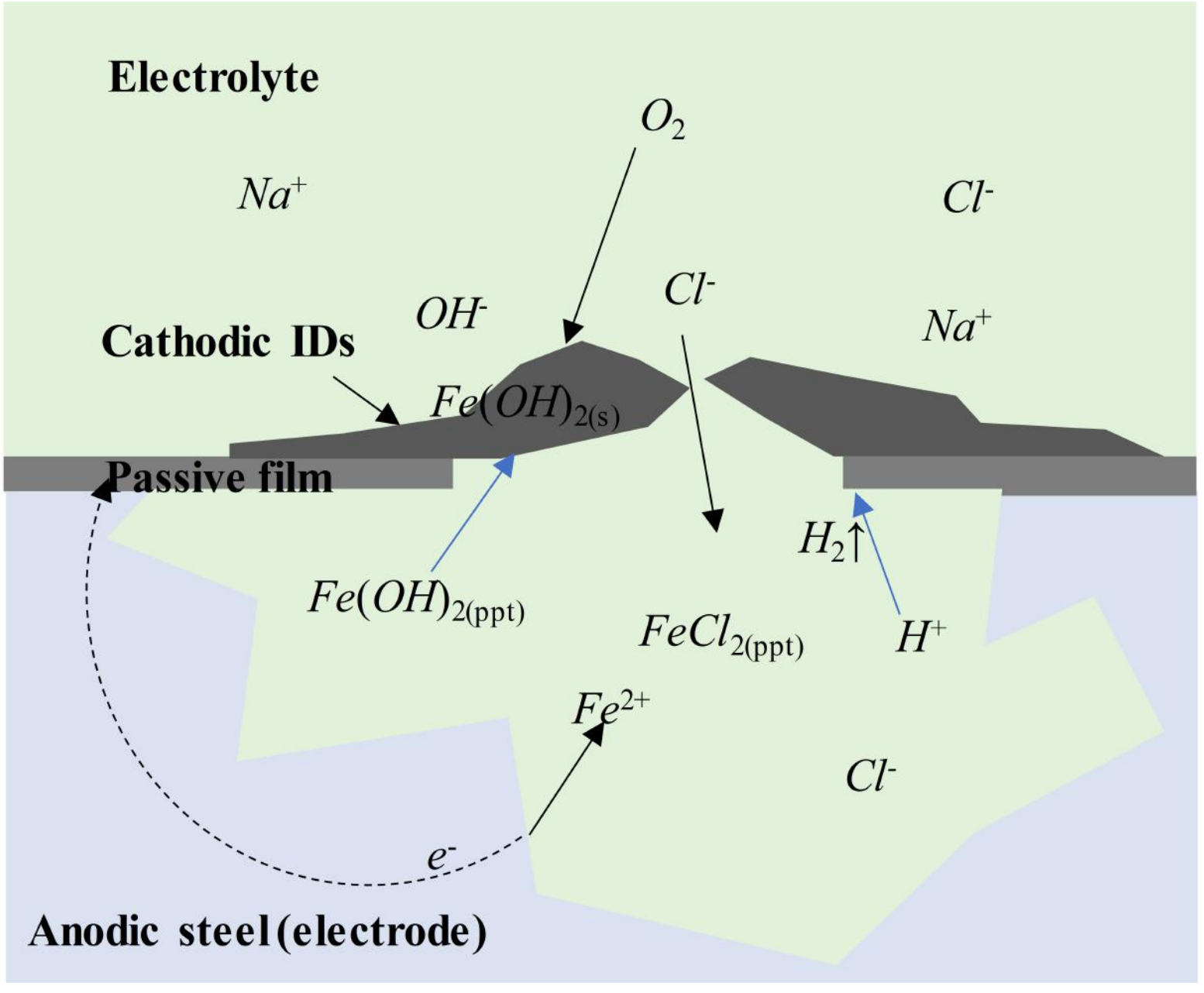
Electrolyte
O_2
Na^+
Cl^-
OH^-
Cl^-
Na^+
Cathodic IDs
$Fe(OH)_{2(s)}$
Passive film
$H_2\uparrow$
$Fe(OH)_{2(ppt)}$
$FeCl_{2(ppt)}$
H^+
Fe^{2+}
Cl^-
e^-
Anodic steel(electrode)

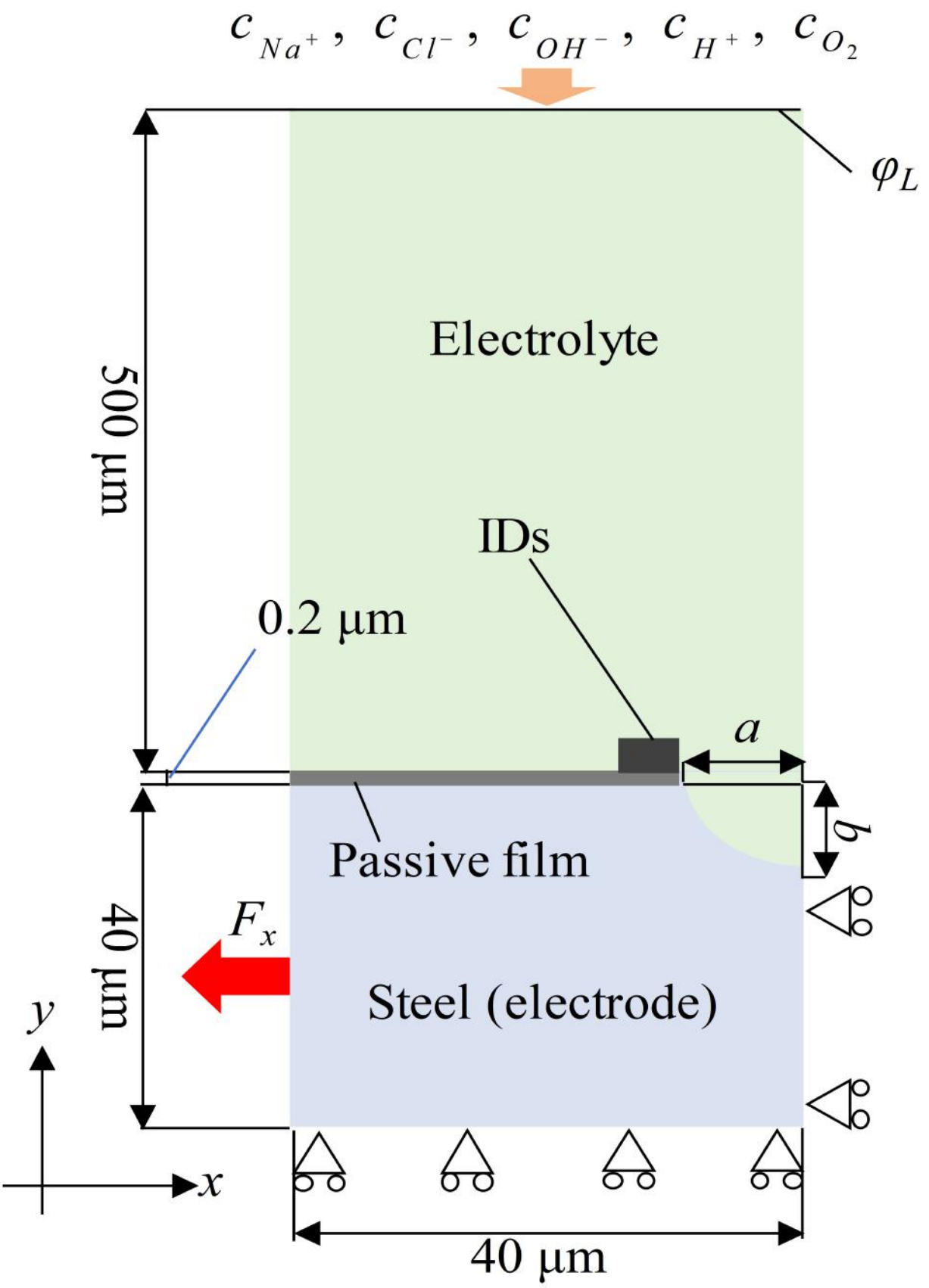
c_{Na^+}, c_{Cl^-}, c_{OH^-}, c_{H^+}, c_{O_2}
φ_L
Electrolyte
500 μm
IDs
0.2 μm
a
b
Passive film
F_x
40 μm
Steel (electrode)
y
x
40 μm

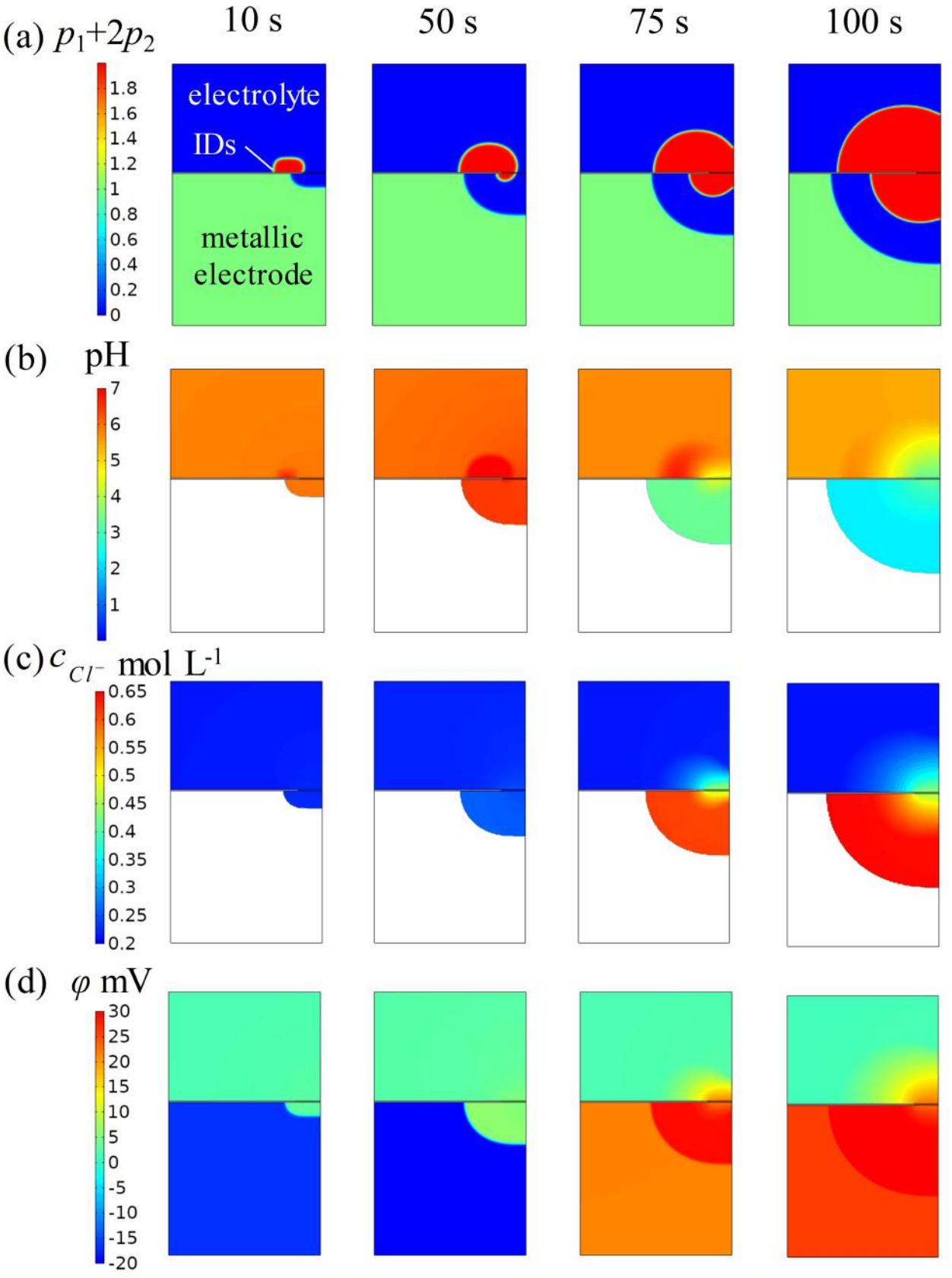
10 s
50 s
75 s
100 s
(a) p_1+2p_2
1.8
1.6
1.4
1.2
1
0.8
0.6
0.4
0.2
0
electrolyte
IDs
metallic
electrode
(b) pH
7
6
5
4
3
2
1
(c) c_{Cl^-} mol L^{-1}
0.65
0.6
0.55
0.5
0.45
0.4
0.35
0.3
0.25
0.2
(d) φ mV
30
25
20
15
10
5
0
-5
-10
-15
-20

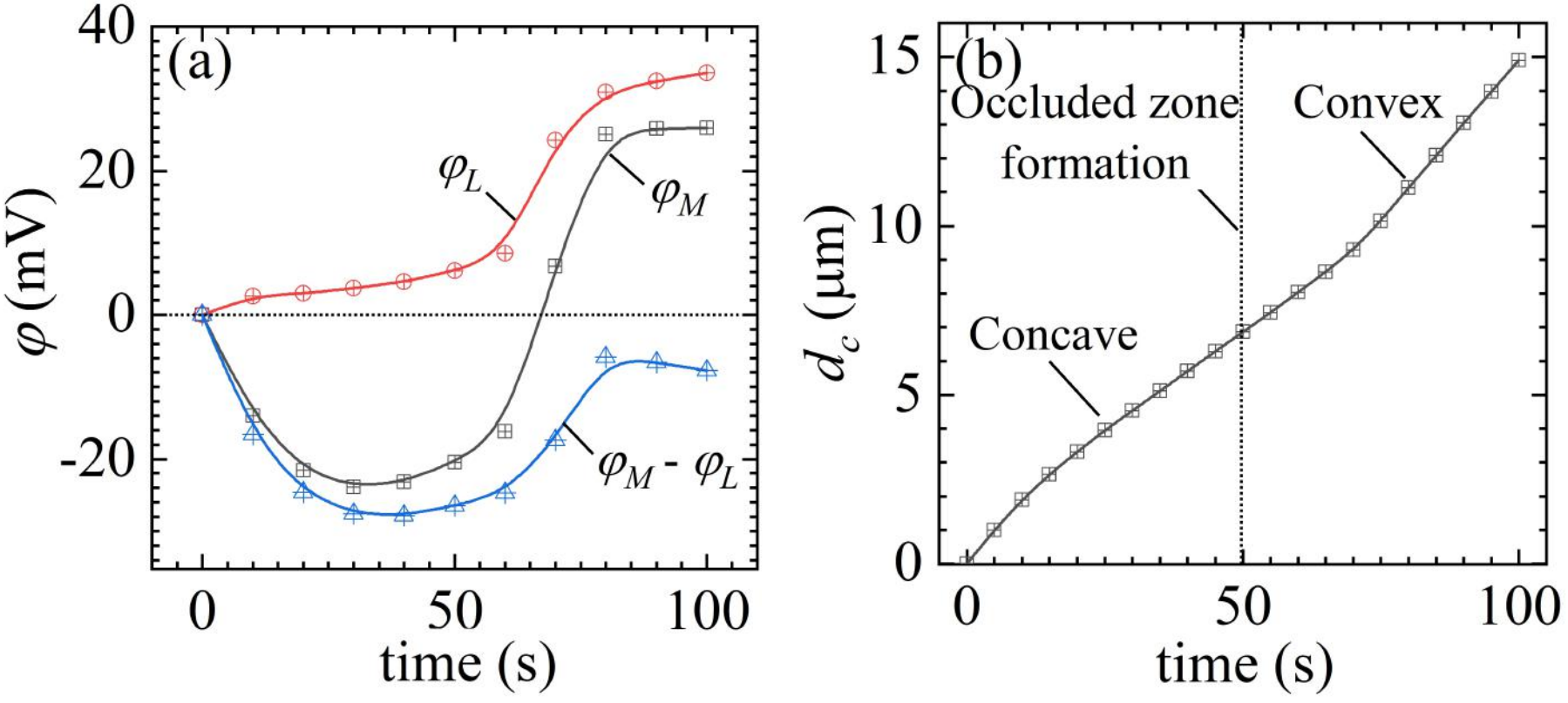
(a)
40
20
0
-20
φ (mV)
φL
φM
φM - φL
0
50
100
time (s)
(b)
15
10
5
0
dc (μm)
Occluded zone
formation
Convex
Concave
0
50
100
time (s)

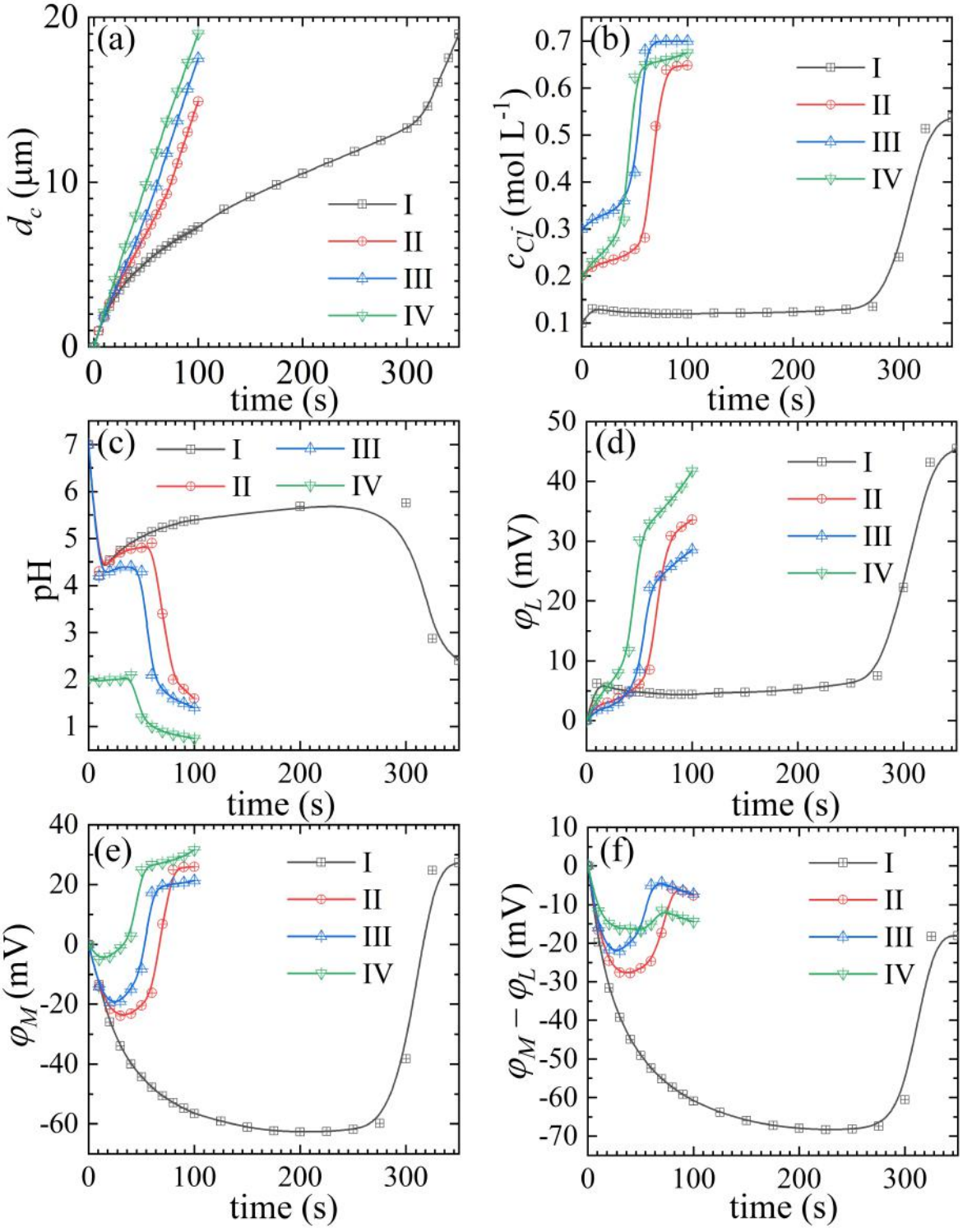
(a)
d_c (μm)
time (s)
I
II
III
IV
(b)
c_{Cl^-} (mol L^{-1})
time (s)
I
II
III
IV
(c)
pH
time (s)
I
II
III
IV
(d)
φ_L (mV)
time (s)
I
II
III
IV
(e)
φ_M (mV)
time (s)
I
II
III
IV
(f)
$\varphi_M - \varphi_L$ (mV)
time (s)
I
II
III
IV

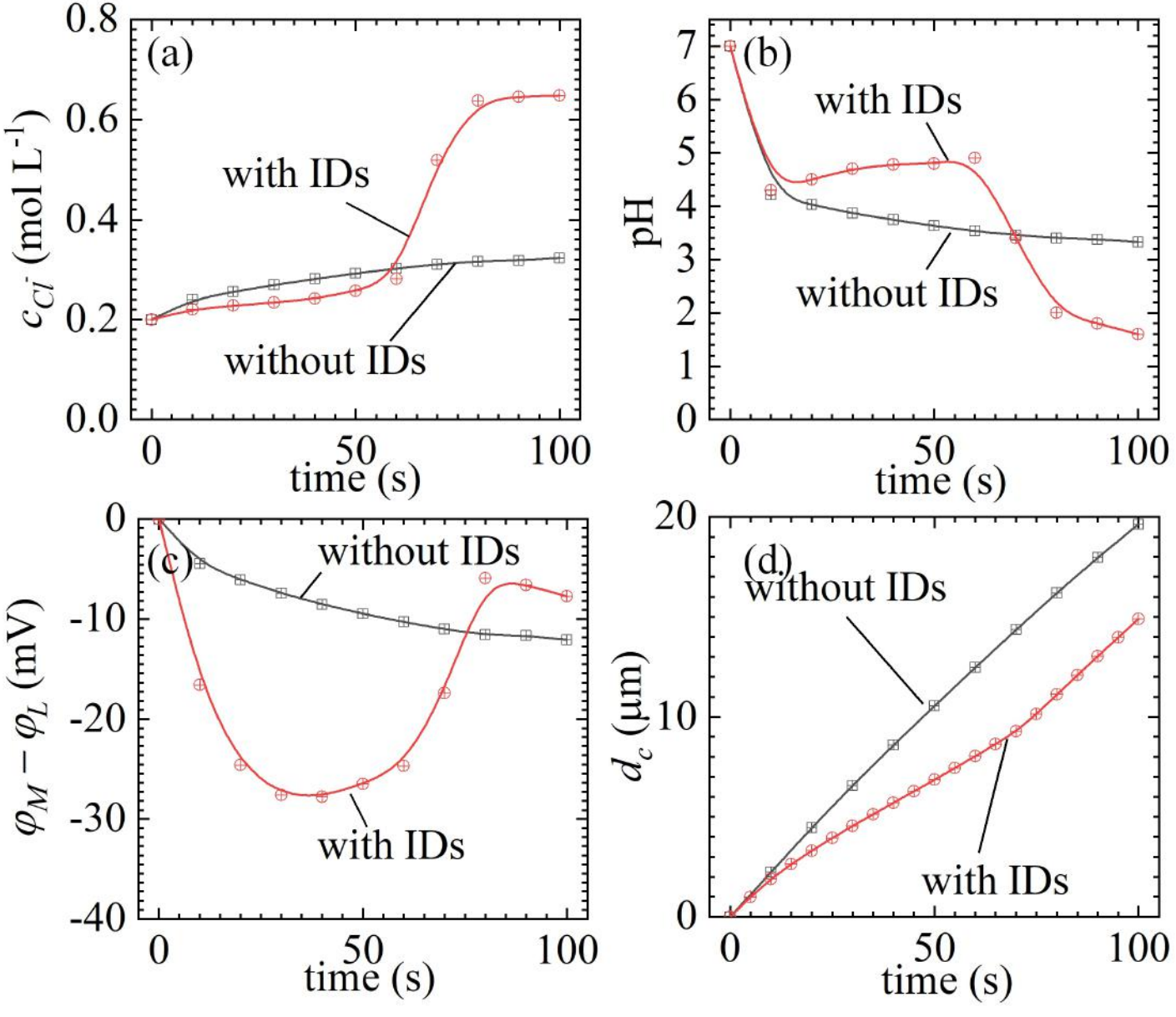
(a)
c_{Cl^-} (mol L^{-1})
0.0
0.2
0.4
0.6
0.8
with IDs
without IDs
0
50
100
time (s)
(b)
pH
0
1
2
3
4
5
6
7
with IDs
without IDs
0
50
100
time (s)
(c)
$\varphi_M - \varphi_L$ (mV)
0
-10
-20
-30
-40
without IDs
with IDs
0
50
100
time (s)
(d)
d_c (μm)
0
10
20
without IDs
with IDs
0
50
100
time (s)

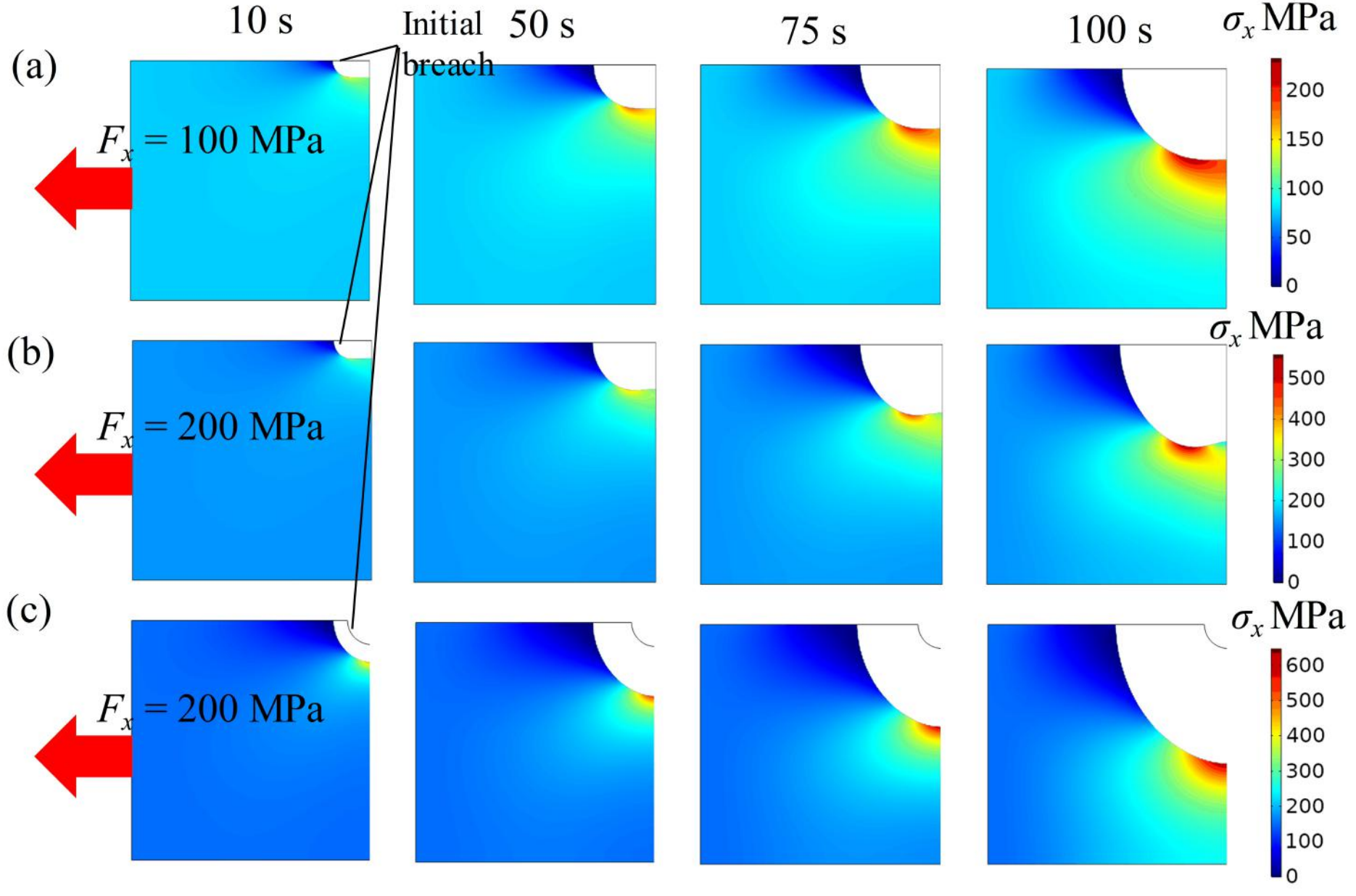
10 s
Initial breach
50 s
75 s
100 s
σ_x MPa
(a)
F_x = 100 MPa
200
150
100
50
0
(b)
F_x = 200 MPa
σ_x MPa
500
400
300
200
100
0
(c)
F_x = 200 MPa
σ_x MPa
600
500
400
300
200
100
0

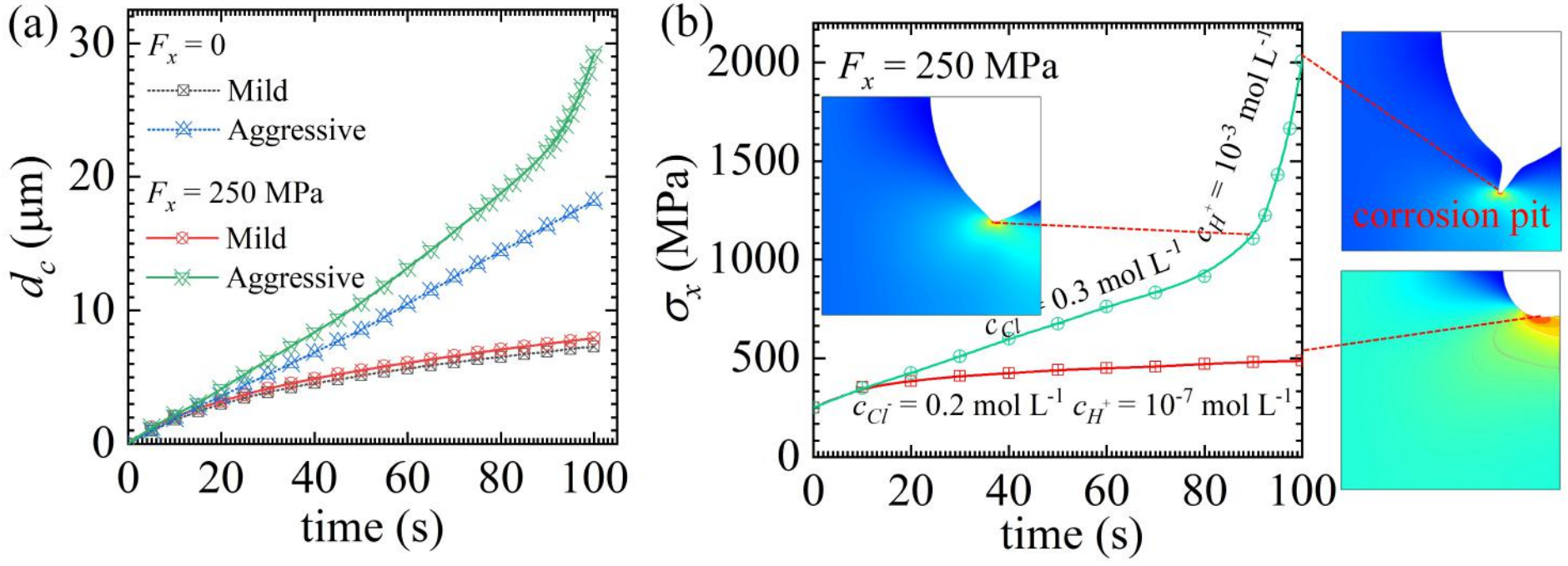
(a)
F_x = 0
Mild
Aggressive
F_x = 250 MPa
Mild
Aggressive
d_c (μm)
time (s)
(b)
F_x = 250 MPa
σ_x (MPa)
time (s)
c_{Cl^-} = 0.3 mol L^{-1}
c_{H^+} = 10^{-3} mol L^{-1}
c_{Cl^-} = 0.2 mol L^{-1} c_{H^+} = 10^{-7} mol L^{-1}
corrosion pit

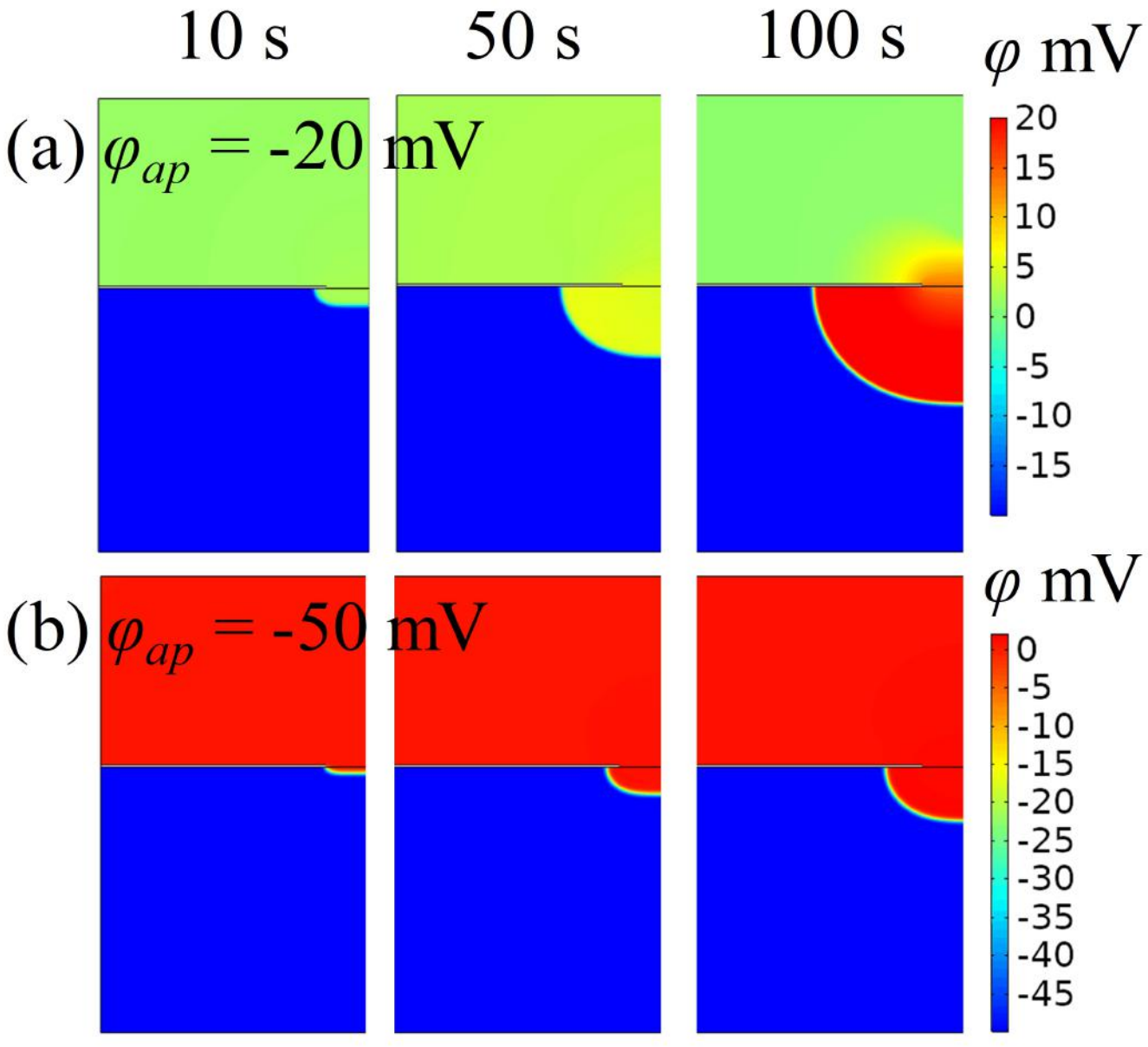
10 s
50 s
100 s
φ mV
(a) φap = -20 mV
20
15
10
5
0
-5
-10
-15
(b) φap = -50 mV
φ mV
0
-5
-10
-15
-20
-25
-30
-35
-40
-45

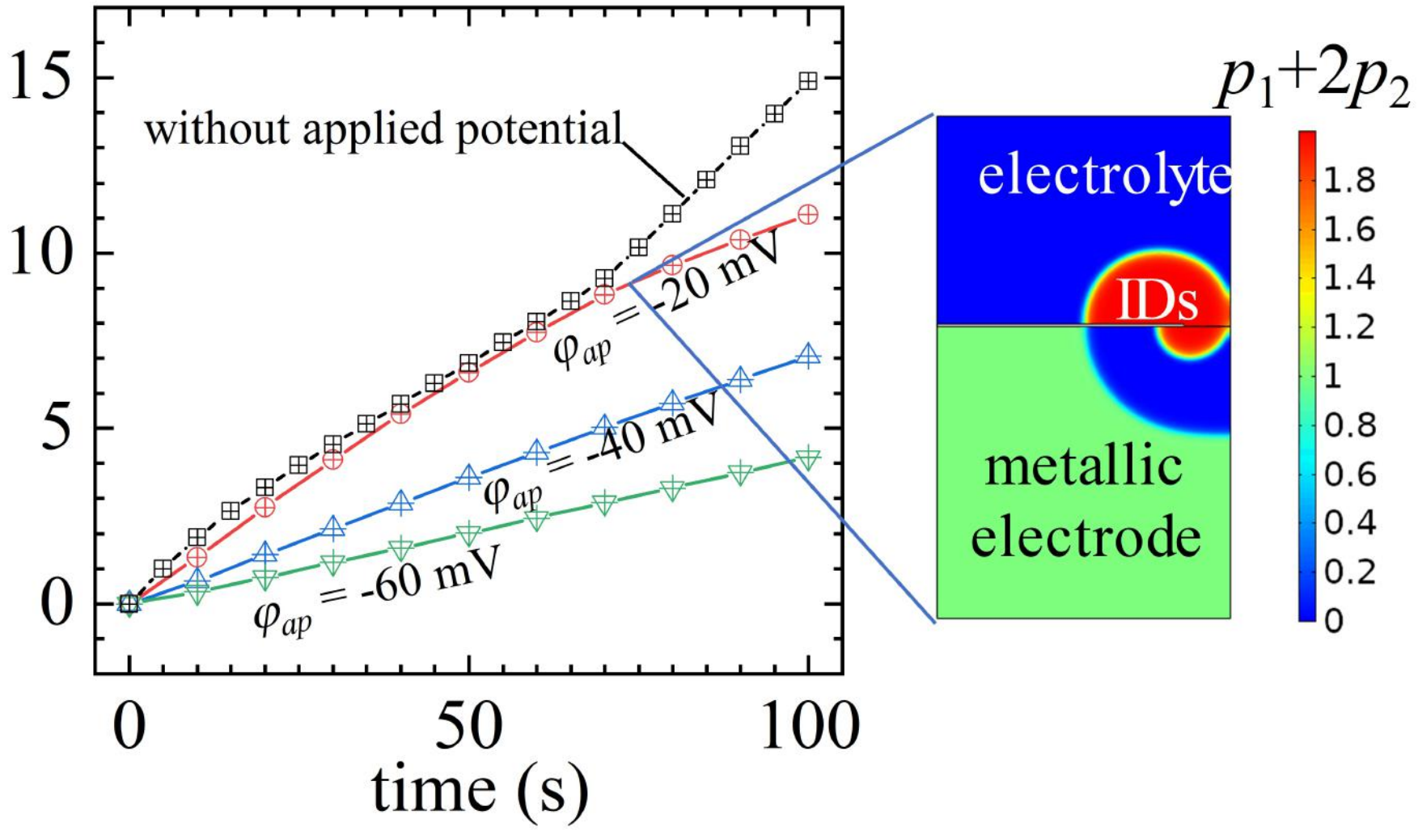
15
10
5
0
0
50
100
time (s)
without applied potential
φ_{ap} = -20 mV
φ_{ap} = -40 mV
φ_{ap} = -60 mV
p_1+2p_2
electrolyte
IDs
metallic
electrode
1.8
1.6
1.4
1.2
1
0.8
0.6
0.4
0.2
0

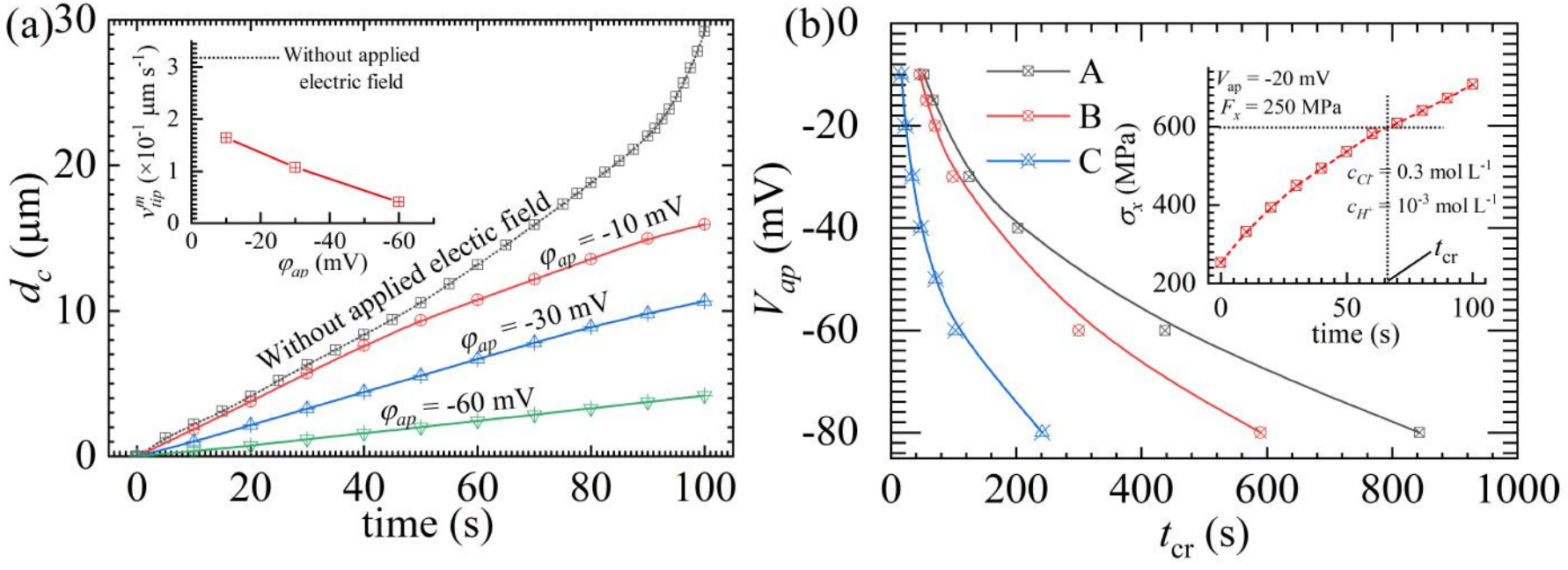
(a)
d_c (μm)
time (s)
Without applied electic field
φ_{ap} = -10 mV
φ_{ap} = -30 mV
φ_{ap} = -60 mV
Without applied electric field
v_{tip}^m (×10^{-1} μm s^{-1})
φ_{ap} (mV)
(b)
V_{ap} (mV)
t_{cr} (s)
A
B
C
σ_x (MPa)
V_{ap} = -20 mV
F_x = 250 MPa
c_{Cl^-} = 0.3 mol L^{-1}
c_{H^+} = 10^{-3} mol L^{-1}
t_{cr}
time (s)

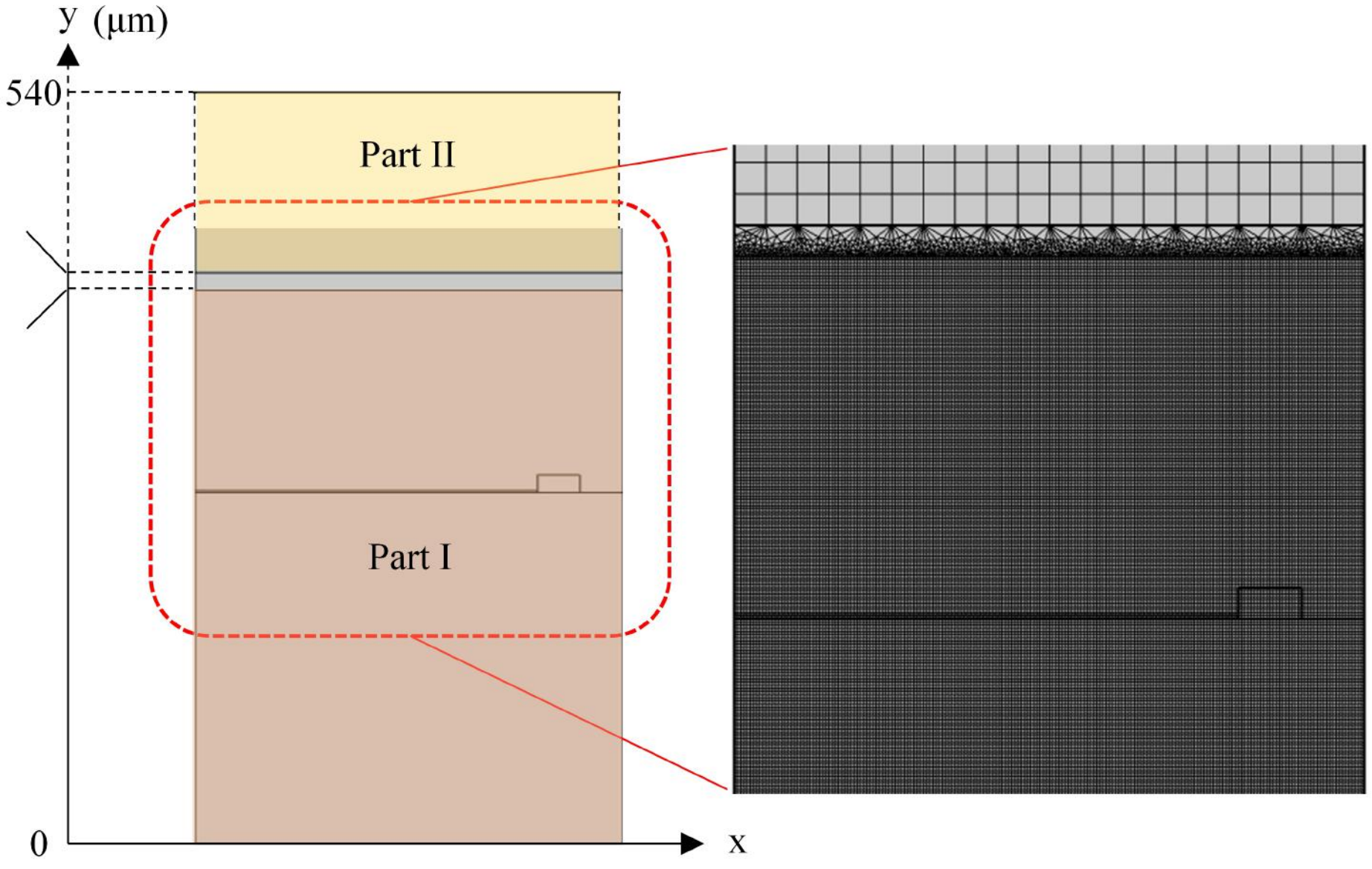
y (μm)
540
Part II
Part I
0
x

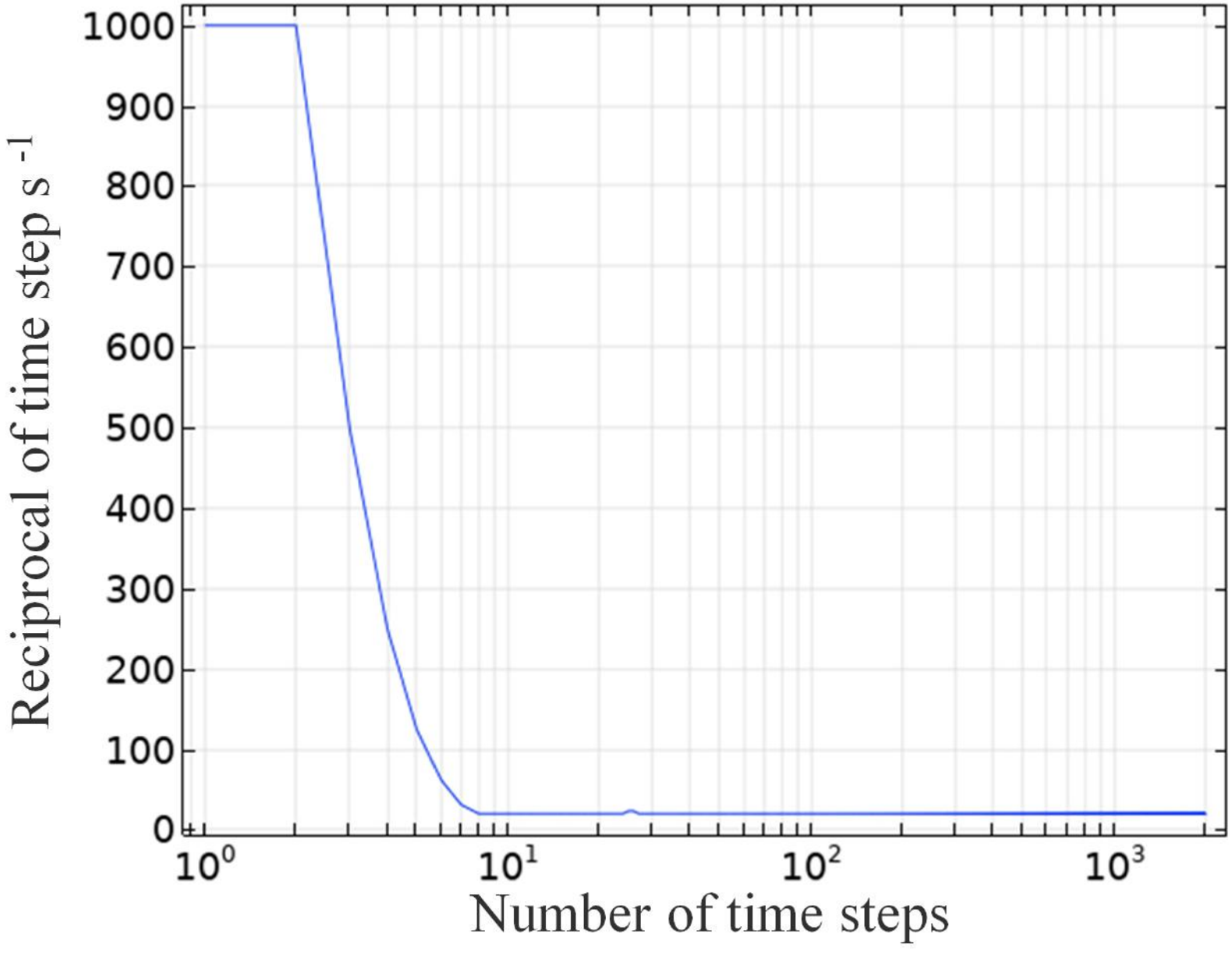
Reciprocal of time step s -1
1000
900
800
700
600
500
400
300
200
100
0
10^0
10^1
10^2
10^3
Number of time steps

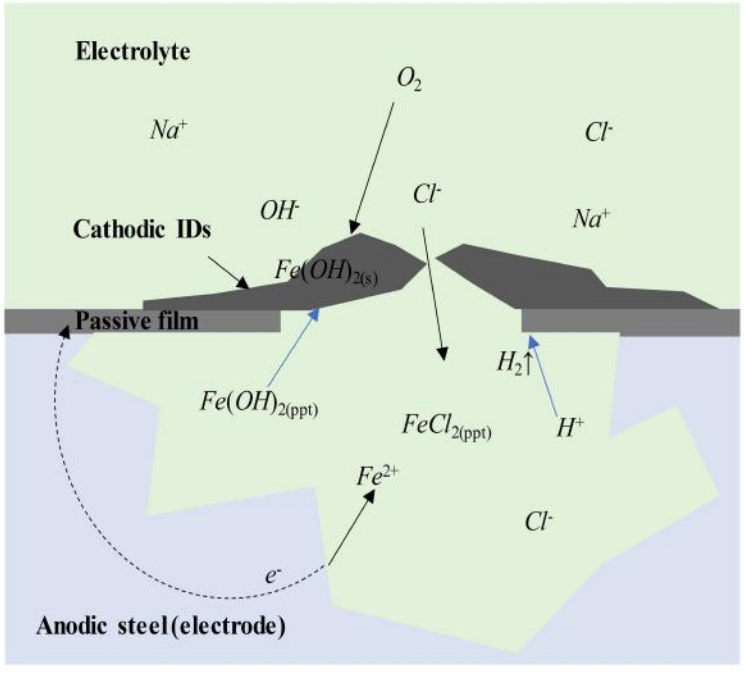

Formation of occluded corrosion cell

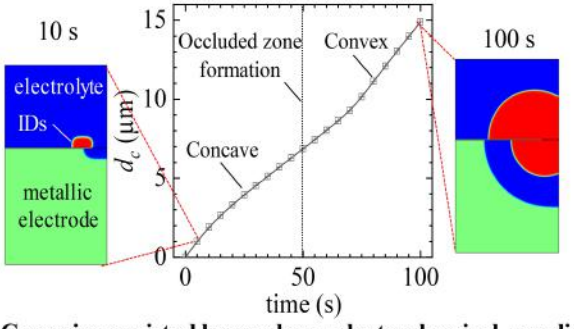

Corrosion assisted by mechano-electrochemical coupling

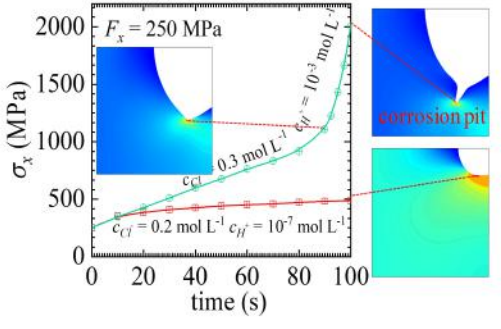

Corrosion arrested by cathodic protection

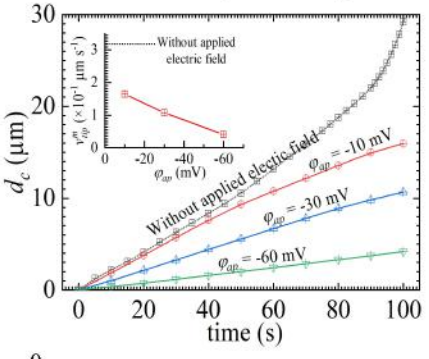

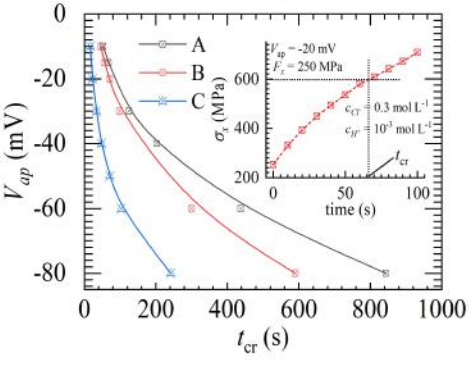

Declaration of interests

 The authors declare that they have no known competing financial interests or personal relationships that could have appeared to influence the work reported in this paper.

☐The authors declare the following financial interests/personal relationships which may be considered as potential competing interests:

Author Statement

Dr Lin was responsible for the (1) ideation (2) PF model establishment (3) simulation implementation (4) original-writing; Dr Lin, Prof. Ruan was responsible for manuscript (1) discussion (2) writing-review and (3) writing-editing.